
NUMERICAL ARTIFACTS IN LEARNING DYNAMICAL SYSTEMS

Bing-Ze Lu

National Chung Cheng University, Taiwan

Richard Tsai

The University of Texas at Austin, USA

ABSTRACT

In many applications, one needs to learn a dynamical system from its solutions sampled at a finite number of time points. The learning problem is often formulated as an optimization problem over a chosen function class. However, in the optimization procedure, it is necessary to employ a numerical scheme to integrate candidate dynamical systems and assess how their solutions fit the data. This paper reveals potentially serious effects of a chosen numerical scheme on the learning outcome. In particular, our analysis demonstrates that a damped oscillatory system may be incorrectly identified as having "anti-damping" and exhibiting a reversed oscillation direction, despite adequately fitting the given data points.

Keywords Dynamical system learning · numerical integrator · numerical stability

1 Introduction

In numerous applications, such as robotics [8][9][25][12], autonomous driving [19][21], and pharmacokinetics and medical applications [18][20], it is necessary to extract some understanding of a complex evolutionary process from time-snapshots of the states. We will refer to this kind of task as dynamical system learning.

Consider autonomous dynamical systems

$$\frac{dy}{dt} = f(y) \in \mathbb{R}^d, \quad (1)$$

where f is a Lipschitz function. Our main goal is to study the potentially non-negligible effects in identifying f from observations of $y(t)$ when a numerical integrator with an insufficiently small step size is used as the forward solver.

Denote $\phi_t[f]y_0$ as the flow of (1) that propagates the initial condition y_0 to time t . Thus, the solution of the differential equation at time t , starting with initial condition y_0 , is denoted as $y(t; y_0) \equiv \phi_t[f]y_0$.

We assume that observations of the trajectories are sampled with a uniform frequency $1/H$, forming the dataset $\mathcal{D}_N = \{(t_n, y(t_n) + \epsilon_n)\}_{n=1}^N$, where $t_n \equiv nH$ and ϵ_n are zero-mean noise in the observations.

We formulate the learning problem as the following least squares fitting problem:

$$\min_{\hat{f} \in \mathcal{F}} \frac{1}{NM} \sum_{y_0 \in U_M} \sum_{n=1}^N |\phi_{t_n}[\hat{f}]y_0 - y(t_n) - \epsilon_n|^2, \quad (2)$$

where \mathcal{F} is a functional class in which we look for f , and U_M contains M sample initial conditions.

In practice, one typically approximates ϕ_t by using a numerical integrator with a step size h . We denote the propagator of the integrator by $S_h[\hat{f}]$. This practice leads to the least squares fitting problem that we shall focus on in this paper:

$$\min_{\hat{f} \in \mathcal{F}} \frac{1}{NM} \sum_{y_0 \in U_M} \sum_{n=1}^N |S_h^{mn}[\hat{f}]y_0 - y(t_n) - \epsilon_n|^2, \quad (3)$$

where $mh = H$. In this paper, we also consider linear multistep methods, for which the associated $S_h[\hat{f}]$ necessarily depends more than just a single initial state. However, for simplicity in our presentation in this section, we will present our discussion of one-step methods.

Denote the global minimizer of (3) by g . Strictly speaking, one has at hand a discrete-time dynamical system defined by the involved numerical scheme and g :

$$y_{n+1} := S_h[g]y_n. \quad (4)$$

We distinguish two driving motivations for solving (3):

1. Use $S_h[g]$ to generate simulated data, extract information, and make inferences about the originally observed dynamical system (1);
2. Analyze and simulate the continuous-time dynamical system

$$\frac{dy}{dt} = g(y); \quad (5)$$

and make inferences about the originally observed dynamical system (1).

We are interested in understanding how to address the following questions:

- Q1 *What if I use a smaller step size or higher order numerical integrator in computing new simulations?*
- Q2 *What is the “generalization” to initial data that is out of the original sampled distribution?*

With a fixed f and y_0 , by solving the optimization problem (3), one constructs an approximation of the flow $\phi_t[f]y_0$, a function of one variable with the constraint defined by the chosen numerical scheme. In this context, comparing $S_h^n[g]y_0$ and $\phi_{t_n}[f]y_0$ for t_n beyond the last observation time amounts to assessing how effective the numerical-scheme-based constraint is for extrapolation. *It is essential to understand how different g and f can be, depending on S_h , the chosen integrator using step size h .*

In Figure 1, we compare a fully resolved trajectory of a system “learned” from trajectory snapshots of a damped nonlinear pendulum. The function class \mathcal{F} in (3) consists of sufficiently expressive Multi-Layer Perceptrons. A fourth-order Runge-Kutta scheme is used to compute solutions of the candidate dynamical system during “training”. While the data is fitted well with an arbitrarily chosen uniform sampling above the Nyquist rate, the fully resolved trajectory reveals that the learned dynamical system is expansive, instead of dissipative!

This is the central question that we address in this paper:

What happens when the chosen numerical integrator uses a step size outside its stability region to identify the unknown dynamical system?

Q2 is a tough question for nonlinear dynamical systems. Generally speaking, approximating f , a function in an infinite-dimensional function space, from finite observations of a small number of trajectories without additional constraints, is challenging, if not ill-posed. However, addressing this issue is essential for learning nonlinear dynamical systems, even for stable systems having limiting cycles or attractors. Indeed, depending on the chosen numerical integrator, orbital trajectories may converge to limit cycles, fixed points, or simply diverge. We present two numerical studies using two model nonlinear oscillators in Section 4.

In most parts of this paper, we consider (1) to be a diagonalizable linear system:

$$f(y) = Ay = PAP^{-1}y, \tag{6}$$

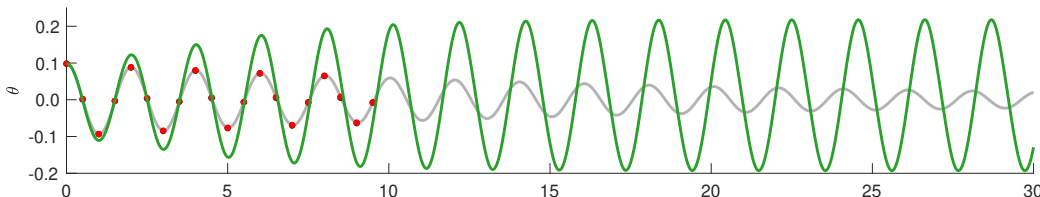


Figure 1: The gray curve shows the angle profile of the underlying damped pendulum dynamics. The red dots along the curve represent the sampled data prepared for training, while the black dots depict the fitted data obtained using the fourth-order Runge–Kutta method with a time step size of h . The green line illustrates the high-resolution solution for the trajectory of the learned dynamics.

and assume that we know the P . It suffices to study the impact of a numerical integrator in learning the scalar equation

$$\frac{dz}{dt} = \lambda z \in \mathbb{C}, \quad (7)$$

where λ is an eigenvalue of f . Thus, our analysis applies to Spectral methods for a broad class of time-dependent partial differential equations.

Our analysis covers two primary classes of numerical integrators: one-step methods and linear multistep methods. For systems with $\text{Re}(\lambda) \leq 0$, we show that the optimal solution, $\hat{\lambda}h$, will always lie in the closure of the stability region of the involved one-step integrator using a fixed step size h to fit noise-data sampled from a trajectory of (7). The case for linear multistep methods is more complicated; $\hat{\lambda}$ does not necessarily lie in their region of absolute stability. However, at least one of the roots of the characteristic polynomials lies within the unit disc on the complex plane.

The implications of these observations include:

- Numerical integrators whose stability regions overlap the right half complex plane may lead to $\hat{\lambda}$ having a positive real part. This fact explains the result shown in Figure 1;
- Linear multistep methods are, in general, more sensitive to perturbation of initial data, due to excitation of spurious roots of the corresponding characteristic polynomials;
- Following the previous points, the Implicit trapezoidal and Implicit midpoint rules are more suitable for learning non-expansive dynamical systems.

Related works

Relating numerical schemes to learning. The Inverse Modified Differential Equations (IMDE) method, introduced in [38], which built upon the modified differential equation framework proposed in [4], provides a robust tool for evaluating learned dynamics by expanding g_θ as a power series in the step size h . This method characterizes a differential equation whose numerical solution matches the sampled data at each sampling time. Additionally, in [39], a comprehensive analysis using the IMDE method is presented to study linear multistep methods in dynamic learning problems. Although the IMDE method provides an asymptotic quantitative error estimation for the learned dynamics, a gap remains in understanding the difference between the trajectory structure of the learned dynamics and the actual dynamics.

In [32], the authors connect learning outcomes to the stability region in Runge-Kutta methods (RKs). They pointed out the non-uniqueness in learning the scalar equations. In this paper, we show that such non-uniqueness can be eliminated by judiciously selecting the right root of the characteristic polynomial.

Their work acknowledges how the stability region of the numerical integrator affects the learned dynamics. However, their conclusion leaves room to explain why higher-order methods can learn incorrect trajectory structures.

In [15, 10] the authors study the stability of the discrete dynamical systems defined by linear multistep methods fitting observations of a dynamical system's trajectory and right-hand side. They proved that the learned discrete process, $S_h[g]$, defined via Adams-Moulton methods, or higher-order Adams-Bashforth methods, are unstable.

Koopman theory and learning dynamical systems

The *Koopman theory* [17] offers a linear perspective on nonlinear dynamical systems by shifting attention from the evolution of states to the evolution of *observables*. Rather than studying the nonlinear flow $\phi_t(y)$ for (1), one investigates the action of the *Koopman operator* \mathcal{K}_t , defined on scalar-valued functions $g: \mathbb{R}^d \rightarrow \mathbb{C}$ by

$$\mathcal{K}_t g(y) := g(\phi_t(y)).$$

Even though f may be nonlinear, the Koopman operator \mathcal{K}_t is linear on the infinite-dimensional space of observables. This enables spectral analysis of nonlinear dynamics by leveraging the linear structure of \mathcal{K}_t .

An *eigenfunction* φ_j of the Koopman operator satisfies

$$\mathcal{K}_t \varphi_j(y) = \varphi_j(\phi_t(y)) = e^{\lambda_j t} \varphi_j(y),$$

for some complex eigenvalue $\lambda_j \in \mathbb{C}$. Along any trajectory $y(t)$, the value of the eigenfunction evolves as

$$\frac{d}{dt}\varphi_j(y(t)) = \lambda_j\varphi_j(y(t)) \iff \varphi_j(y(t)) = e^{\lambda_j t}\varphi_j(y(0)).$$

This exponential evolution can be derived using the chain rule:

$$\frac{d}{dt}\varphi_j(y(t)) = \nabla\varphi_j(y(t)) \cdot \frac{dy(t)}{dt} = \nabla\varphi_j(y(t)) \cdot f(y(t)).$$

Thus, one derives the equation for the generator of the Koopman semigroup:

$$\nabla\varphi_j(y) \cdot f(y) = \lambda_j\varphi_j(y). \quad (8)$$

Koopman’s framework has been extended beyond measure-preserving systems, as in [24, 23], allowing application to a broad class of dissipative and driven systems. In practical settings, the Koopman operator is approximated by projecting it onto a finite-dimensional basis of observables. This results in a matrix representation whose eigenvalues and eigenvectors approximate those of \mathcal{K}_t . Techniques such as Extended Dynamic Mode Decomposition (EDMD) rely on this approach.

However, the quality of these approximations critically depends on the choice of basis functions. Poorly chosen bases can lead to inaccurate or ill-posed approximations, particularly when the dynamics are chaotic or when the data is noisy.

In the context of *learning dynamical systems*, Koopman theory inspires a family of lifting-based methods that seek to embed nonlinear dynamics into a space where the evolution is approximately linear. Our analysis is highly relevant to these approaches.

SINDy The Sparse Identification of Nonlinear Dynamics (SINDy) algorithm [3] selects a suitable g from a dictionary of candidates to fit data that includes both $y(t_n)$ and the vector field $f(y(t_n))$. A key idea is to convert the nonlinear identification task into solving a linear equation $Ax = b$. Here, the matrix A is formed by column-wise stacking of candidate functions, with each row representing the function’s value at a particular time instance, while b records the system’s first-order derivative. The authors in [37] provide a rigorous analysis of the algorithm’s convergence and demonstrate that these results apply to many SINDy-related methods. For further extensions, [13] shows that there is a high probability of accurately recovering the learned function, represented as a multivariate polynomial, even when outliers, dependencies, and noise corrupt the collected data. [30] and [31] explore the application of compressive sensing to propose several sampling strategies for extracting governing equations from high-dimensional dynamic data, addressing the

ill-posedness that arises when the number of (noisy) observations is smaller than the number of unknowns.

Neural ODEs Deep learning strategies are popular for constructing approximations of the vector fields, f , from observations. For example, [22] employs a neural network with added stochastic effects to model molecular kinetics, while [33] introduces a more sophisticated structure using long-short-term memory gates to uncover dynamic behavior. Additionally, [34] leverages autoencoders to approximate the true dynamics from data, and [36] presents a deep learning approach to identify a proximal propagating operator within a given function space. See [2], [16], [27] for extensive discussions.

Many related articles adopt this notion to create their neural networks. Specifically, [5] utilizes a one-step numerical integrator to solve (5), where a neural network determines g_θ . In contrast, [5], [35], and [28] apply linear multistep methods as their numerical integrators in the learning process. These approaches emphasize determining a g_θ rather than interpreting the system's physical nature. Recognizing this limitation, [11] proposed an HNNet that advances the field by focusing on dynamics that preserve energy. An improvement is made in [6], confirming that the symplectic integrators perform numerically better than other methods. There are also discussions about learning dynamics using implicit methods, such as those presented in [29][26]. See [14] for a more extensive survey of applications.

The outline of the paper

In Section 2, we study one-step methods for learning the model equation (7). In Section 3, we study the use of linear multistep methods. In Section 4, we present some numerical studies, involving linear PDEs and nonlinear oscillators, that verify the theories presented in Sections 2 and 3. Finally, we conclude in Section 5.

2 Linear systems learning with one-step methods

This section explores the learned dynamics inferred by data using one-step methods. We will qualitatively analyze the behavior of the learned dynamics and connect the results to the theory of absolute stability. We first analyze the learning outcomes using noise-free observed data and then extend the discussion to noisy data.

One-step methods for scalar linear equations with constant step size h evolve the numerical solution by multiplying the characteristic polynomial $p(\xi)$, where $\xi = \lambda h$. The numerical solution after n steps is given by $z_n = p(\xi)^n z_0$.

The characteristic polynomial $p(\xi)$ depends on the time-stepping scheme:

$$\text{Forward Euler: } p(\xi) = 1 + \xi, \quad (9)$$

$$\text{Backward Euler: } p(\xi) = \frac{1}{1 - \xi}, \quad (10)$$

$$\text{Explicit Runge–Kutta (order } k\text{): } p(\xi) = \sum_{j=0}^k \frac{\xi^j}{j!}, \quad k = 2, 3, 4. \quad (11)$$

We also include the Implicit Trapezoidal rule, whose characteristic polynomial is given by:

$$\text{Implicit Trapezoidal Rule: } p(\xi) = \frac{1 + \frac{1}{2}\xi}{1 - \frac{1}{2}\xi}. \quad (12)$$

In the following discussion, we use the notation Z_n to represent the observed data. In particular, $Z_n = e^{\lambda(nh)} Z_0$ is the exact solution of (7) with initial data Z_0 at time $t = nh$. Meanwhile, we use z_n to represent the numerical solution at the n th iteration step with step size h , starting from $z_0 = Z_0$.

In this section, we analyze the global minimizer of least squares problems defined as follows:

$$\min_{\xi \in \mathbb{C}} \frac{1}{N} \sum_{k=1}^N |z_{mk} - Z_0 e^{\lambda m h k}|^2 \quad \text{s. t. } z_{mk} = p(\xi)^{mk} z_0, \quad (13)$$

where $p(\xi)$ is a characteristic function of a one-step integrator defined in (9)-(11) and mh is the sampling step size with m being a positive integer. Figure 2 depicts the loss landscapes defined by (13) for the Forward Euler, RK2, and implicit trapezoidal discretizations. The global minimum is zero in these cases, but the RK2 landscape reveals multiple distinct points that achieve this optimum.

The following Lemma characterizes the global minimizers.

Lemma 2.1. *Let $\hat{\lambda}$ be the minimizer of (13). For any positive h , there exists $\hat{\lambda}h \in \mathbb{C}$ satisfying*

$$p(\hat{\lambda}h) = e^{\lambda h}. \quad (14)$$

Furthermore, $\xi^ = \hat{\lambda}h$ is the global minimizer to (13) with which the objective function to reach its global minimum 0.*

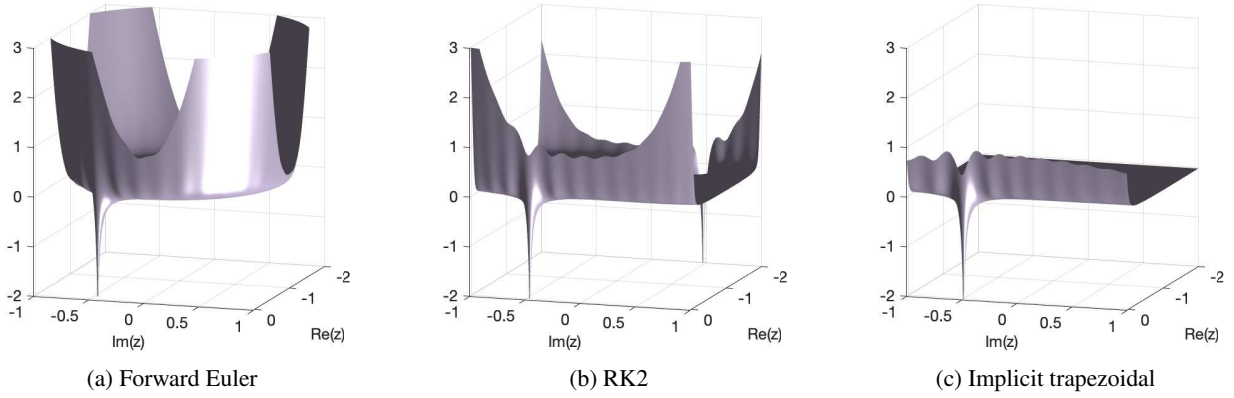


Figure 2: The landscape of objective functions with different numerical methods in the complex plane to learn $\lambda h = (-5 - 2\pi i)/32$. The z axis is labeled on a logarithmic scale, while the x and y axes correspond to the imaginary and real axes.

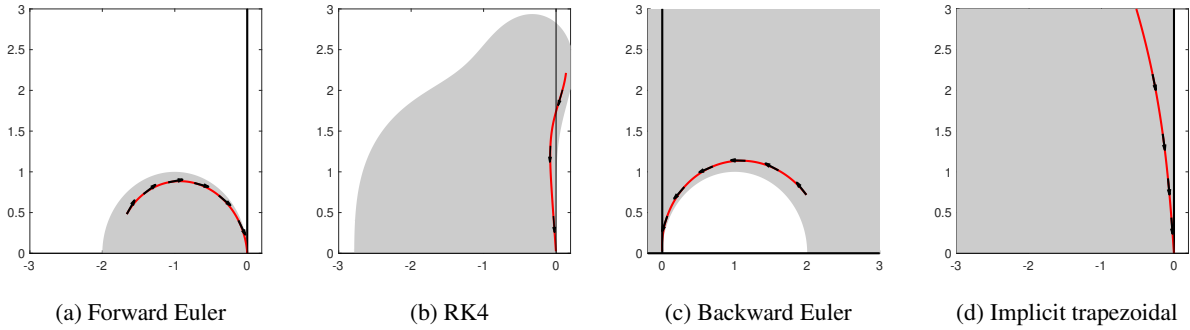


Figure 3: Profiles of the learned quantity $\hat{\lambda}h$ using the Forward Euler, Backward Euler, RK4, and implicit trapezoidal methods as h varying from 0 to 0.2. The true $\lambda = -1 + 4\pi i$ is set. Red curves show how $\hat{\lambda}h$ moves within each method's stability region; arrows point toward the limit as $h \rightarrow 0$.

Proof. (i) Explicit Runge-Kutta methods, including Forward Euler:
By the Fundamental Theorem of Algebra, for any given $\lambda h \in \mathbb{C}$,

$$p(\xi) - e^{\lambda h} = 0$$

has a solution on the complex plane.

(ii) Now consider Backward Euler and Implicit Trapezoidal Rule:

- $(1 - \xi)e^{\lambda h} = 1$ [Backward Euler],
- $(1 - \frac{1}{2}\xi)e^{\lambda h} - (1 + \frac{1}{2}\xi) = 0$ [Implicit Trapezoidal method].

Since $e^{\lambda h} \neq 0$, it is clear that each equation has a unique solution. Denote the solution as $\xi^* = \hat{\lambda}h$. Clearly, for $z_0 = Z_0$,

$$\frac{1}{N} \sum_{k=1}^N |p(\xi)^{mk} z_0 - Z_0 e^{\lambda m h k}|^2 = 0$$

is a global minimum. □

Figure 3 compares the paths of optimal $\hat{\lambda}h$ as $h \rightarrow 0^+$ for different one-step methods and their stability regions. In the following subsections, we will provide more explicit characterizations of the signs of $\text{Re}(\hat{\lambda})$ and $\text{Im}(\hat{\lambda})$ relative to λh .

2.1 One-step method for conservative dynamics

Based on Lemma 2.1, we may relate the global minimizer of the least squares, the step size used in the numerical integrator, to the integrator's stability region.

The following theorem clarifies the errors in the amplitude and the rotation direction of the identified dynamical system using one-step methods.

Theorem 2.1. *Assume that $\text{Re}(\lambda) = 0$ in (7). Then the global minimum of (13), with S_h^n being one-step methods, is attained at $\hat{\lambda}$ satisfying*

$$|p(\hat{\lambda}h)| = |e^{\lambda h}| = 1.$$

Furthermore, the $\hat{\lambda}h$ resides on the boundary of the selected numerical method's stability region.

In the following, we present our analysis of a few chosen one-step methods. The results concerning the sign of $\text{Re}(\hat{\lambda})$ are summarized in Table 1. The readers can find the detailed proofs in the Appendix. A natural prerequisite of our results is that the step size h has to be sufficiently small so that at least two data points are observed for each period of the oscillation.

Definition 2.1 (Nyquist condition for λh). *Given $z' = \lambda z$ for some $\lambda \in \mathbb{C}$. We say that λh meets the Nyquist condition when*

$$-\pi < \text{Im}(\lambda h) < \pi. \tag{15}$$

The first Corollary states that one will identify a dissipative system with the Forward Euler method.

Corollary 2.1 (Characterization of $\hat{\lambda}$ learned by Forward Euler method). *Assume that λh meets the Nyquist condition (2.1) and $h > 0$. Let $\hat{\lambda}$ be the global minimizer of (13), with the evolution operator S_h^n given by the Forward Euler method. Then the following properties hold:*

- $\text{Re}(\hat{\lambda}) < 0$,
- $\text{sign}(\text{Im}(\hat{\lambda})) = \text{sign}(\text{Im}(\lambda))$.

The next Corollary states that with the RK2 or RK3 method, the learned dynamics may be expansive!

Corollary 2.2 (Characterization of $\hat{\lambda}$ learned by Runge–Kutta methods). *Assume that λh meets the Nyquist condition (2.1), $h > 0$, and that the following conditions hold for the respective Runge-Kutta schemes:*

$$[\text{RK2}] \quad |1 - e^{\lambda h}| \leq \frac{1}{2},$$

$$[\text{RK3}] \quad |1 - e^{\lambda h}| \leq \frac{1}{6}.$$

Then the global minimizer $\hat{\lambda}$ of (13), with S_h^n given by the corresponding Runge–Kutta method, satisfies

$$|\hat{\lambda}h| \leq 1.$$

Moreover, $\hat{\lambda}$ has the following properties:

$$\text{sign}(\text{Im}(\hat{\lambda})) = \text{sign}(\text{Im}(\lambda)),$$

and

$$[\text{RK2}] \quad \text{Re}(\hat{\lambda}) < 0,$$

$$[\text{RK3}] \quad \text{Re}(\hat{\lambda}) > 0.$$

The third Corollary in this subsection establishes that Backward Euler *will always lead to an expansive system*, while in contrast, the Implicit Trapezoidal Rule will lead to learning conservative dynamical systems.

Corollary 2.3 (Characterization of $\hat{\lambda}$ learned by Implicit methods). *Assume that λh meets the Nyquist condition (2.1) and $h > 0$. Let $\hat{\lambda}$ be the global minimizer of (13), with S_h^n given by either the Backward Euler method or the implicit trapezoidal rule. Then the following properties hold:*

$$\text{sign}(\text{Im}(\hat{\lambda})) = \text{sign}(\text{Im}(\lambda)),$$

and

$$[\text{Backward Euler}] \quad \text{Re}(\hat{\lambda}) > 0,$$

$$[\text{Implicit Trapezoidal}] \quad \text{Re}(\hat{\lambda}) = 0.$$

Table 1: The difference between dynamics $\hat{\lambda}$ learned from different numerical methods, while the true dynamics λ are either dissipative $\text{Re}(\lambda) < 0$ or conservative $\text{Re}(\lambda) = 0$. The trapezoidal rule effectively preserves the structural trends of the true dynamics across different methods.

| $y' = \lambda y$ | $\text{Re}(\lambda) = 0$ | $\text{Re}(\lambda) < 0$ |
|----------------------|---|--------------------------------|
| Forward Euler | $\text{Re}(\hat{\lambda}) < 0$ | $\text{Re}(\hat{\lambda}) < 0$ |
| RK2 | $\text{Re}(\hat{\lambda}) < 0$ | $\text{Re}(\hat{\lambda}) < 0$ |
| RK3 | $\text{Re}(\hat{\lambda}) > 0$ (for $0 < h \ll 1$) | Cond. Dissipative |
| Backward Euler | $\text{Re}(\hat{\lambda}) > 0$ | Cond. Dissipative |
| Implicit Trapezoidal | $\text{Re}(\hat{\lambda}) = 0$ | $\text{Re}(\hat{\lambda}) < 0$ |

2.2 One-step method for dissipative dynamics

In this subsection, we focus on the case where the true dynamic system is dissipative, that is, $\text{Re}(\lambda) < 0$.

Theorem 2.2. *Assume that $\text{Re}(\lambda) < 0$ in (7). Then the global minimum $\hat{\lambda}h$ of (13), with S_h^n being a one-step method, lies on the level set $\{z \in \mathbb{C} : |p(z)| = |e^{\lambda h}|\} \subset \{z \in \mathbb{C} : |p(z)| < 1\}$. Furthermore, $\hat{\lambda}h$ resides in the selected numerical method's stability region.*

Note that as $h \rightarrow 0$, the learned dynamic approaches the stability region's locus, making the shape of the stability region crucial in dynamic learning problems.

Corollary 2.4 (Characterization of $\hat{\lambda}$ learned by Forward Euler method). *Assume that λh meets the Nyquist condition (2.1) and $h > 0$. Let $\hat{\lambda}$ be the global minimizer of (13), with the evolution operator S_h^n given by the Forward Euler method. Then the following properties hold:*

- $\text{Re}(\hat{\lambda}) < 0$,

Table 2: Sign of $\text{Im}(\hat{\lambda}h)$ for one-step methods, inferred from data $e^{\lambda h} = e^{a+i\theta}$.

| Method/Data type | Data with damping ($a < 0$) | Purely oscillatory data ($a = 0$) |
|-------------------|---|--|
| Forward Euler | $\text{Im}(\hat{\lambda}h) = e^a \sin \theta$ lagging phase | $\text{Im}(\hat{\lambda}h) = \sin \theta$ small $ \theta \Rightarrow$ small phase error |
| Backward Euler | $\text{Im}(\hat{\lambda}h) = e^{-a} \sin \theta$ leading phase | $\text{Im}(\hat{\lambda}h) = \sin \theta$ small $ \theta \Rightarrow$ small phase error |
| RK2 | $\text{Im}(\hat{\lambda}h) = \frac{e^a \sin \theta}{1 + \text{Re}(\hat{\lambda}h)}$ | $\text{Im}(\hat{\lambda}h) = \frac{\sin \theta}{1 + \text{Re}(\hat{\lambda}h)}$ |
| Impl. Trapezoidal | $\text{Im}(\hat{\lambda}h) = \frac{2e^a \sin \theta}{ e^{\lambda h} + 1 ^2}$ lagging phase | $\text{Im}(\hat{\lambda}h) = \frac{2 \sin \theta}{ e^{\lambda h} + 1 ^2} \approx \theta$ small $ \theta \Rightarrow$ small phase error |

- $\text{sign}(\text{Im}(\hat{\lambda})) = \text{sign}(\text{Im}(\lambda))$.

We analyze the cases using the RK2 and RK3 methods.

Corollary 2.5 (Characterization of $\hat{\lambda}$ learned by Forward Euler method). *Assume that λh meets the Nyquist condition (2.1), $h > 0$, and that one of the following Runge-Kutta-specific conditions holds:*

$$[\text{RK2}] \quad 2|1 - e^{\lambda h}| \leq 1,$$

$$[\text{RK3}] \quad 6|1 - e^{\lambda h}| \leq \delta^2 \text{ and } |e^{\lambda h}| \leq \sqrt{\frac{8}{9}}, \text{ where the parameter } \delta > 0 \text{ satisfies}$$

$$\frac{6 - \delta^2}{2\delta} \geq \sqrt{12.5}.$$

Then the learning objective (13), with time-stepping scheme S_h^n given by the respective Runge-Kutta method, admits a unique global minimizer $\hat{\lambda} \in \mathbb{C}$, which satisfies:

$$[\text{RK2}] \quad |\hat{\lambda}h| \leq 1,$$

$$[\text{RK3}] \quad |\hat{\lambda}h| \leq \delta.$$

Moreover, the minimizer $\hat{\lambda}$ has the following qualitative properties:

$$\text{sign}(\text{Im}(\hat{\lambda})) = \text{sign}(\text{Im}(\lambda)),$$

and

$$[\text{RK2}] \quad \text{Re}(\hat{\lambda}) < 0,$$

$$[\text{RK3}] \quad \text{Re}(\hat{\lambda}) > 0.$$

Similarly, we report the minimizer's properties using the Backward Euler and the Implicit Trapezoidal rule:

Corollary 2.6 (Sign preservation by Implicit methods). *Assume that λh meets the Nyquist condition (2.1) and $h > 0$. Let $\hat{\lambda}$ be the global minimizer of (13), with the evolution operator S_h defined by either the implicit trapezoidal rule or the Backward Euler method. Then the following hold:*

[Implicit Trapezoidal]

$$\text{Re}(\hat{\lambda}) < 0, \quad \text{sign}(\text{Im}(\hat{\lambda})) = \text{sign}(\text{Im}(\lambda)).$$

[Backward Euler] *If $\text{Re}(1 - e^{-\lambda h}) < 0$, then the same conclusion holds:*

$$\text{Re}(\hat{\lambda}) < 0, \quad \text{sign}(\text{Im}(\hat{\lambda})) = \text{sign}(\text{Im}(\lambda)).$$

When the actual dynamics are dissipative, using the Forward Euler and RK2 methods, the stability region lies entirely on the left-hand side of the complex plane, ensuring that the learned dynamics are dissipative and align with the actual dynamics. Conversely, the RK3 method only preserves the dissipative trends conditionally; moreover, if the data is sampled at a finer rate, the learning results will exhibit expansive trends. Compared to the conservative scenario, RK methods generally capture dissipative behavior better in a dissipative setting.

The implicit trapezoidal method consistently preserves dissipative behavior regardless of the step size and retains both conservative and dissipative behaviors, demonstrating its robustness in dynamical learning problems. In contrast, the Backward Euler method cannot definitively ensure a dissipative learned dynamic, making it less suitable for learning problems.

2.3 Phase errors

Let the true solution over one sampling interval be $e^{\lambda h} = e^{a+i\theta}$ with prescribed step size h . We derive formulas for the imaginary part of the learned eigenvalue $\hat{\lambda}h$ and classify the resulting phase errors.

Without loss of generality, $z_0 = Z_0 = 1$. Since the analytical solution of the learned dynamics takes the form $e^{\hat{\lambda}t}$,

$$\text{Im}(\hat{\lambda}h) = \phi(\theta, a) \implies e^{\hat{\lambda}t} = e^{\text{Re}(\hat{\lambda}t)} e^{i\phi(\theta, a)t/h}.$$

So $\phi(\theta, a)$ determines the frequency of oscillations in the learned dynamics, and the phase errors relative to the actual dynamics.

If $|\phi(\theta, a)| > |\theta|$, the learned dynamics has faster oscillations, and we say that the phases in the learned dynamics are “leading.” Otherwise, we say that the phases are “lagging.”

Consider the Forward Euler method. By Lemma 2.1, each discrete step with step length h should be precisely $e^{\lambda h}$:

$$1 + \hat{\lambda} = e^{(a+i\theta)} \implies \text{Im}(\hat{\lambda}h) = e^a \sin(\theta).$$

Thus, *dissipation/damping in the actual dynamics, i.e., $a < 0$, leads to slower oscillations in the learned dynamics.*

In contrast, for the Backward Euler method, we have

$$\frac{1}{1 - \hat{\lambda}h} = e^{a+i\theta} \implies \text{Im}(\hat{\lambda}h) = e^{-a} \sin \theta.$$

Without dissipation, i.e. $a = 0$, the Backward Euler method will yield identical lagging phase errors (albeit different amplitudes). However, dissipation in the actual dynamics *accelerates* the oscillations in the learned dynamics inferred by the Backward Euler. See Figure 4. See also Section 4.2 for an example involving a convection-diffusion equation.

The amplitude error and the phase error in the systems inferred by different numerical schemes are summarized in Table 1 and Table 2.

2.4 Richardson’s extrapolation

In this section, we show that Richardson extrapolation combined with the Implicit Trapezoidal Rule preserves the system’s non-expansivity for any positive step size, while simultaneously improving the asymptotic accuracy of the learned dynamics.

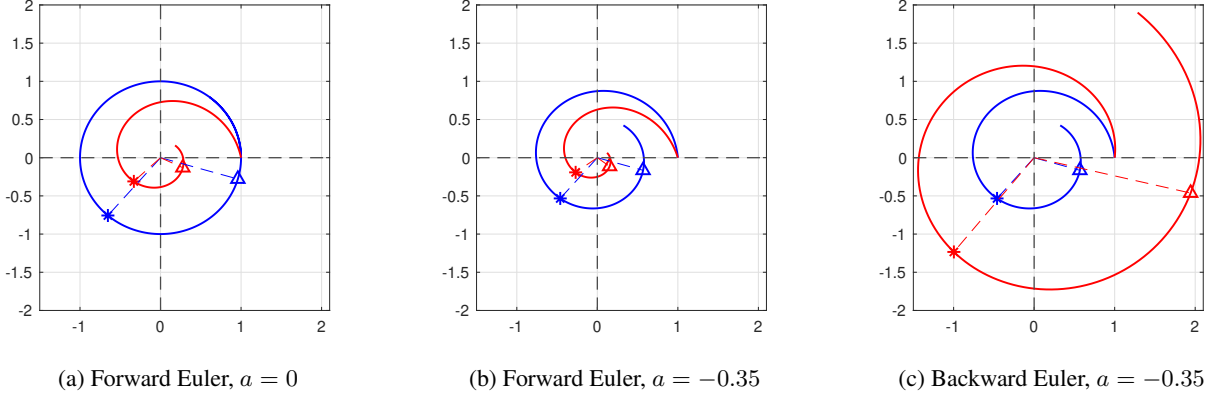


Figure 4: Phase errors in the dynamics learned by Forward and Backward errors. Dissipation (characterized by a negative value for a) in the actual dynamical system acts as the opposite of the learned system – dissipation slows down the oscillations in the system learned by the Forward Euler method. The blue curves correspond to the actual trajectory, and the red ones are the fully resolved trajectories of the learned systems. The positions of the solutions at two different times are shown by \diamond 's and \triangle 's.

Theorem 2.3 (Extrapolation with Implicit Trapezoidal Rule). *Assume that $\text{Re}(\lambda) = 0$. Let $\hat{\lambda}_h$ and $\hat{\lambda}_{2h}$ denote the learned eigenvalues obtained by solving (13) using the implicit trapezoidal rule with step sizes h and $2h$, respectively. Define*

$$\hat{\lambda}_{exp} := \frac{4}{3}\hat{\lambda}_h - \frac{1}{3}\hat{\lambda}_{2h}.$$

Then

$$|\hat{\lambda}_{exp} - \lambda| = \mathcal{O}(h^4).$$

Moreover, if

$$\text{Im}(\lambda h) \in \left(-4 \tan^{-1} \left(\sqrt{\frac{1}{3}(11 - 4\sqrt{7})} \right), 4 \tan^{-1} \sqrt{\frac{1}{3}(11 - 4\sqrt{7})} \right) \subset \left(-\frac{\pi}{2}, \frac{\pi}{2} \right),$$

then the extrapolated value satisfies:

- $\text{Re}(\hat{\lambda}_{exp}) = 0$,
- $\text{sign}(\text{Im}(\hat{\lambda}_{exp})) = \text{sign}(\text{Im}(\lambda))$.

Proof. Recalling the asymptotic expansion of the learned dynamic using step size h :

$$\hat{\lambda}_h = \lambda - \frac{\lambda^3}{12}h^2 + \frac{\lambda^5}{12}h^4 + \mathcal{O}(h^6).$$

For step size $2h$, we have:

$$\hat{\lambda}_{2h} = \lambda - \frac{\lambda^3}{12}(2h)^2 + \frac{\lambda^5}{12}(2h)^4 + \mathcal{O}(h^6).$$

Applying the extrapolation formula:

$$3\hat{\lambda}_{\text{exp}} = 4\hat{\lambda}_h - \hat{\lambda}_{2h} = 3\lambda - 8\frac{\lambda^5}{12}h^4 + \mathcal{O}(h^6).$$

Next, we analyze the real and the imaginary part of the extrapolated dynamic $\hat{\lambda}_{\text{exp}}$.

Real part

The learned dynamic $\hat{\lambda}_h$ using sampling timestep h follows

$$\hat{\lambda}_h = \frac{2e^{\lambda h} - 1}{he^{\lambda h} + 1} = \frac{2}{h} \tanh\left(\frac{\lambda h}{2}\right).$$

By hypothesis, $\text{Re}(\lambda h) = 0$, we have $\text{Re}(\hat{\lambda}_h) = 0$, then

$$\text{Re}(\hat{\lambda}_{\text{exp}}) = \frac{4}{3}\text{Re}(\hat{\lambda}_h) - \frac{1}{3}\text{Re}(\hat{\lambda}_{2h}) = 0.$$

Imaginar part

Recall the imaginar part of the learned dynamic $\hat{\lambda}_h$,

$$\text{Im}(\hat{\lambda}_h) = \frac{4}{h} \tan\left(\frac{\text{Im}(\lambda h)}{2}\right).$$

If $\text{Im}(\lambda h) \in \left(-4 \tan^{-1}\left(\sqrt{\frac{1}{3}(11 - 4\sqrt{7})}\right), 4 \tan^{-1}\sqrt{\frac{1}{3}(11 - 4\sqrt{7})}\right) \subset \left(-\frac{\pi}{2}, \frac{\pi}{2}\right)$, then the extrapolated dynamic

$$\text{sign}(\hat{\lambda}_{\text{exp}}h) = \text{sign}(\lambda h),$$

by direct computation. □

The following theorem generalizes Theorem 2.3 to those true dynamic $\text{Re}(\lambda) < 0$.

Theorem 2.4. *Assume that $\text{Re}(\lambda) < 0$, let λ_h and λ_{2h} be the learned dynamic solving (13) using the implicit trapezoidal method with sampling timestep h and $2h$ respectively.*

Let $a := \text{Re}(\lambda h)$ and $b := \text{Im}(\lambda h)$ denote the real and the imaginary part of λh respectively.

Suppose

$$a \leq -\cosh^{-1}\left(\sqrt{256/223}\right), \quad b \in \left(0, \frac{\pi}{2}\right) \text{ or}$$

$$-\cosh^{-1}(\sqrt{256/223}) < a < 0 < b < \cos^{-1}\left(\frac{\cosh a + \sqrt{256 - 223 \cosh^2 a}}{16}\right),$$

then the extrapolated value satisfies

- $\operatorname{Re}(\hat{\lambda}_{\text{exp}}) < 0$,
- $\operatorname{sign}\left(\operatorname{Im}(\hat{\lambda}_{\text{exp}})\right) = \operatorname{sign}(\operatorname{Im}(\lambda))$.

Proof. Recall the learned dynamic satisfies the equation $\hat{\lambda}_h = \frac{2}{h} \tanh\left(\frac{\lambda h}{2}\right)$.

By using the expression

- $\operatorname{Re}(\tanh(a + bi)) = \frac{\sinh(2a)}{\cosh(2a) + \cos(2b)}$,
- $\operatorname{Im}(\tanh(a + bi)) = \frac{\sin(2b)}{\cosh(2a) + \cos(2b)}$.

We can explicitly express the real and the imaginary parts of the extrapolated dynamic $\hat{\lambda}_{\text{exp}} = \frac{4}{3}\lambda_h - \frac{1}{3}\lambda_{2h}$:

- $\operatorname{Re}(\hat{\lambda}_{\text{exp}}) = \frac{4}{3} \left(\frac{2}{h} \frac{\sinh(a)}{\cosh(a) + \cos(b)} \right) - \frac{1}{3} \left(\frac{2}{2h} \frac{\sinh(2a)}{\cosh(2a) + \cos(2b)} \right)$.
- $\operatorname{Im}(\hat{\lambda}_{\text{exp}}) = \frac{4}{3} \left(\frac{2}{h} \frac{\sin(a)}{\cosh(a) + \cos(b)} \right) - \frac{1}{3} \left(\frac{2}{2h} \frac{\sin(2a)}{\cosh(2a) + \cos(2b)} \right)$.

If

$$a \leq -\cosh^{-1}(\sqrt{256/223}), \text{ and } b \in \left(0, \frac{\pi}{2}\right)$$

or

$$-\cosh^{-1}(\sqrt{256/223}) < a < 0 < b < \cos^{-1}\left(\frac{\cosh a + \sqrt{256 - 223 \cosh^2 a}}{16}\right),$$

then, by direct computation, we have $\operatorname{Re}(\hat{\lambda}_{\text{exp}}) < 0$ and $\operatorname{sign}\left(\operatorname{Im}(\hat{\lambda}_{\text{exp}})\right) = \operatorname{sign}(\operatorname{Im}(\lambda))$. \square

2.5 Noisy data

In this section, we examine how noise in the data influences the learning problem:

$$\begin{aligned} \min_{\xi \in \mathbb{C}} \frac{1}{N} \sum_{k=1}^N |z_k - (Z_0 e^{\lambda h k} + \epsilon_k)|^2, \\ \text{s. t. } z_k = p(\xi)^k (Z_0 + \epsilon_0), \quad k = 0, 1, \dots, N, \end{aligned} \quad (16)$$

where $p(\xi)$ is the characteristic polynomial of a one-step method and ϵ_k denotes the noise added to the noise-free observation $Z_0 e^{\lambda h k}$.

Theorem 2.5. *Let $\hat{\lambda}h$ be the minimizer of (16) for noise-free data ($\epsilon_k \equiv 0$, $k = 1, \dots, N$), and let λ^*h be the minimizer when the data are perturbed by complex noises $\{\epsilon_k\}_{k=1}^N$ with $|\epsilon_k| \leq \sigma$. Assume*

1. $|p(\lambda^*h)| \leq M$;
2. for every $\theta \in [0, 1]$ and $\eta = \theta \hat{\lambda} + (1 - \theta)\lambda^*$,

$$|p(\eta h)|^k |p'(\eta h)| \geq c_0 > 0, \quad \forall k, \quad (17)$$

where c_0 is independent of k and σ .

Then there exists a constant $C = C(Z_0, M, c_0)$ such that

$$|\lambda^*h - \hat{\lambda}h|^2 \leq C \sigma^2. \quad (18)$$

The proof can be found in the Appendix section 6.4.

According to this theorem, if the actual dynamic is conservative, the learned dynamic will lie near the boundary of the stability region.

3 Linear systems learning with linear multistep methods

Linear multistep methods (LMMs) for the scalar differential equation, $\frac{dz}{dt} = \lambda z$, take the general form:

$$\sum_{j=0}^k \alpha_j z_{n+j} = \lambda h \sum_{j=0}^k \beta_j z_{n+j}, \quad \alpha_k = 1, \quad (19)$$

with the given initial conditions

$$z_j = Z_0 e^{j\lambda h}, \quad j = 0, 1, 2, \dots, k-1. \quad (20)$$

For example, the Leap-Frog scheme:

$$z_{n+2} = z_n + 2\lambda h z_{n+1}. \quad (21)$$

We will refer to the Backward Difference Methods as BDF k , and Adams methods as AB k and AM k , where k indicates the number of steps used by the scheme. In the appendix, we provide the coefficients for the schemes analyzed in this paper.

Define the characteristic polynomial of a linear multistep method

$$\pi_{\lambda h}(z) := \rho(z) - \lambda h \kappa(z) = 0, \quad (22)$$

where

$$\rho(z) = \sum_{j=0}^k \alpha_j z^{n-j}, \text{ and } \kappa(\xi) = \sum_{j=0}^k \beta_j z^{n-j}. \quad (23)$$

For the given λh , if the roots are unique, the solution of the recurrence relation (19) has the general form

$$z_n = \sum_{j=1}^k c_j \zeta_j^n. \quad (24)$$

If a root ζ_j has a multiplicity μ , then the general solution will include terms of the form

$$n^\nu \zeta_j^n, \quad \nu = 0, 1, 2, \dots, \mu - 1.$$

In standard practices, the coefficients c_1, \dots, c_k are determined by the given initial data: z_0, z_1, \dots, z_{k-1} . We denote $c_j \equiv c_j(\xi; z_0, \dots, z_{k-1})$ to emphasize the smooth dependence on ξ and the initial conditions. Consequently,

$$z_n \equiv z_n(\xi; z_0, \dots, z_{k-1}).$$

For a given ξ , some of the roots may lie outside of the unit disc and some inside. If the given initial conditions lie in the span of those $\zeta_j \equiv \zeta_j(\xi)$ lying strictly inside the unit disc, $|z_n|$ is uniformly bounded for $n \geq 0$. Thus, the stability of z_n is determined by $\xi = \lambda h$ as well as the given initial condition.

The region of absolute stability for an LMM is defined as the set for $\xi = \lambda h$ in which the roots of $\pi_{\lambda h}(z)$ lie within the unit disc on the complex plane; i.e.

$$\mathcal{R}_A := \{\xi \in \mathbb{C} : \text{for any } z \in \mathbb{C} \text{ such that } \rho(z) - \xi \kappa(z) = 0 \implies |z| < 1\}.$$

For dissipative problems, it is crucial to select h so that $\lambda h \in \mathcal{R}_A$. This way, the computation will be stable *for all* possible initial data.

However, the main interest in this paper is in what $\hat{\lambda}h$ would be for a chosen LMM, given a sequence of observations with exponentially decreasing amplitudes.

We consider the learning problem for k -step linear multistep methods as the following constrained optimization problem, in which the data sampling time step $H = mh$ requires m steps ($m > k$) of the integrator using step size h :

$$\left\{ \begin{array}{l} \min_{\xi \in \mathbb{C}} \frac{1}{N} \sum_{n=1}^N |z_{mn}(\xi, c_1, \dots, c_k) - Z_{mn}|^2, \\ \sum_{j=0}^k \alpha_j z_{n+j}(\xi) = \xi \sum_{j=0}^k \beta_j z_{n+j}(\xi), \quad a_k = 1, \quad \text{and} \\ z_j(\xi) = Z_j, \quad j = 0, 1, \dots, k-1, \end{array} \right. \quad (25)$$

where Z_{mn} for $n = 0, 1, \dots, N$, are the observation data, and z_0, z_1, \dots, z_{k-1} are the initial data for the problem; these initial conditions can be interpolated from the observed data points.

For the model problem $z' = \lambda z$, it is equivalent to:

$$\left\{ \begin{array}{l} \min_{\xi \in \mathbb{C}} \frac{1}{N} \sum_{n=1}^N \left| \sum_{j=1}^k c_j \zeta_j^{mn}(\xi) - Z_{mn} \right|^2, \quad n = 1, 2, \dots, N, \\ \sum_{j=1}^k c_j \zeta_j^n(\xi) = Z_n, \quad n = 0, 1, \dots, k-1. \end{array} \right. \quad (26)$$

Note that if $Z_n = \zeta_j^n, j = 0, 1, 2, \dots, k-1$, i.e., then $c_n = 0$ for all $n \neq j$. Conversely, if $Z_n = e^{n\lambda h}$, there exists a $\hat{\xi} = \hat{\lambda}h$ such that $c_n = 0$ for all $n \neq j$.

- If $\text{Re}(\lambda) < 0$, $\hat{\lambda}h$ is **not** necessarily be in \mathcal{R}_A , because the unstable roots cannot contribute to forming the values of z_n to fit the data with exponentially decreasing amplitudes.
- However, when one computes the learned iterations

$$\sum_{j=0}^k \alpha_j z_{n+j} = \hat{\lambda}h \sum_{j=0}^k \beta_j z_{n+j},$$

with initial conditions that excite the unstable roots, the resulting simulation becomes unstable.

- Even if all the characteristic roots, $\zeta_j(\hat{\lambda})$ lie inside the unit disc, $\hat{\lambda}h$ may not! This possibility is evident for those methods whose \mathcal{R}_A overlaps with the right half of the complex plane.

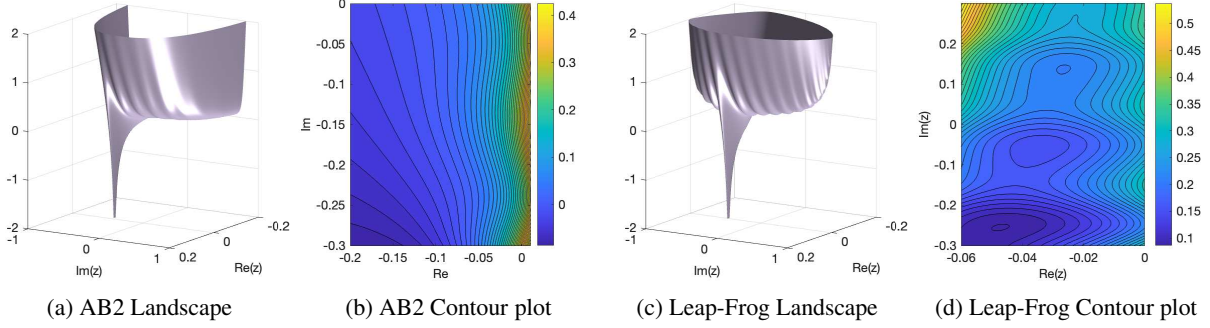


Figure 5: The landscapes of the objective function for the Leap-Frog method and the AB2 method in the complex plane, used to learn $\lambda h = -(0.1 - 5\pi i)/32$. The z -axis in the left panel is shown on a logarithmic scale. The contour plot on the right reveals the presence of many local minima.

In the remainder of this section, we consider the case when the sampling time step is the same as the step size of the numerical scheme, observations have no noise and $Z_0 = 1$; i.e., $m = 1$ and $Z_n = e^{n\lambda h}$.

Figure 5 demonstrates the objective function landscapes defined by (25) induced by AM2, AM2, for $m = 1$ and $Z_n = e^{n\lambda h}$, $n = 0, 1, \dots, N$.

Lemma 3.1. *The global minimum of the learning problem (25), with $m = 1$ and $Z_n = e^{n\lambda h}$, $n = 0, 1, \dots, N$, is attained at*

$$\hat{\xi} = \frac{\rho(e^{\lambda h})}{\kappa(e^{\lambda h})}, \quad (27)$$

and the solution to the recurrence relation matches the analytical solution of the differential equation; i.e. $z_n(\hat{\xi}) = e^{n\lambda h}$.

Proof. Consider the first k terms of the LMMs,

$$\sum_{j=0}^k \alpha_j e^{j\lambda h} = \xi \sum_{j=0}^k \beta_j e^{j\lambda h}, \quad a_k = 1 \quad (28)$$

and it is straightforward to find $\xi = \frac{\sum_{j=0}^k \alpha_j e^{j\lambda h}}{\sum_{j=0}^k \beta_j e^{j\lambda h}} = \frac{\rho(e^{\lambda h})}{\kappa(e^{\lambda h})}$.

Next, the numerical solution at z_{k+1} follows the following formula,

$$\alpha_k z_{k+1} + \sum_{j=0}^{k-1} \alpha_j e^{(j+1)\lambda h} = \xi \left(\beta_k z_{k+1} + \sum_{j=0}^{k-1} \beta_j e^{(j+1)\lambda h} \right) \quad (29)$$

$$= \alpha_k z_{k+1} + e^{\lambda h} \sum_{j=0}^{k-1} \alpha_j e^{j\lambda h} = \xi \left(\beta_k z_{k+1} + e^{\lambda h} \sum_{j=0}^{k-1} \beta_j e^{j\lambda h} \right). \quad (30)$$

$$\text{If } \xi = \frac{\sum_{j=0}^k \alpha_j e^{j\lambda h}}{\sum_{j=0}^k \beta_j e^{j\lambda h}} = \frac{\rho(e^{\lambda h})}{\kappa(e^{\lambda h})},$$

$$\xi \left(e^{\lambda h} \sum_{j=0}^{k-1} \beta_j e^{j\lambda h} \right) = e^{\lambda h} \left(\sum_{j=0}^k \alpha_j e^{j\lambda h} - \xi \beta_k e^{k\lambda h} \right).$$

Thus, we can write the solution at $n = k + 1$ as:

$$\begin{aligned} \alpha_k z_{k+1} + e^{\lambda h} \sum_{j=0}^{k-1} \alpha_j e^{j\lambda h} &= \xi (\beta_k z_{k+1}) + e^{\lambda h} \left(\sum_{j=0}^k \alpha_j e^{j\lambda h} - \xi \beta_k e^{k\lambda h} \right) \\ \Rightarrow \alpha_k (z_{k+1} - e^{\lambda h} e^{k\lambda h}) &= \xi \beta_k (z_{k+1} - e^{\lambda h} e^{k\lambda h}). \end{aligned}$$

Since $\alpha_k - \xi \beta_k \neq 0$, we must have

$$z_{k+1} - e^{\lambda h} e^{k\lambda h} = 0 \Rightarrow z_{k+1} = e^{(k+1)\lambda h}.$$

If ξ is chosen to be $\frac{\rho(e^{\lambda h})}{\kappa(e^{\lambda h})}$, then, by induction, $z_n(\xi) = e^{n\lambda h}$ for all n . \square

Theorem 3.1. *Assume that $\text{Re}(\lambda) = 0$ in (7). If $\hat{\lambda}$ is a global minimizer of (25), with $m = 1$ and $Z_n = e^{n\lambda h}$, $n = 0, 1, \dots, N$, it must lie on the boundary of the numerical method's absolute stability region.*

Proof. Since $\text{Re}(\lambda) = 0$, by Lemma 3.1, $|z_n(\hat{\lambda}h)| \equiv 1$. This means $\hat{\lambda}h \in \partial\mathcal{R}_A$. \square

See Figure 8 that compares $\hat{\lambda}h$ to the region of absolute stability for AB3, AM3, and the Leap-Frog scheme. See Figure 9 that compares $\hat{\lambda}$ and the ground truth λ for various step sizes.

3.1 Analysis of four two-step multistep methods

For two-step methods, we first analyze the co-existence of stable, unstable, and repeated roots by the quadratic formula. We summarize the analysis for four classical two-step methods in Table 3.

Next, with the knowledge of the characteristic roots, we study the optimal parameter, $\hat{\lambda}h$, of the learning problem – under a simpler setup. We consider observation data of $Z_n = \zeta^n$, where

$$\zeta = e^{a+i\theta}, \quad a \leq 0,$$

such that $|Z_n| \leq 1$.

The objective is to determine whether the numerical scheme could inadvertently learn an unstable dynamical system ($\text{Re}(\hat{\lambda}) > 0$), potentially also reversing the direction of oscillations ($\text{Re}(\hat{\lambda}) \text{Re}(\zeta) = -1$). The analysis involves examining the rational function

$$\hat{\lambda}h = \frac{\rho(\zeta)}{\kappa(\zeta)},$$

and is summarized in Table 4.

From the table, we see that AB2 and BDF2 are not generally viable methods for learning dissipative systems with oscillations because of the possibility of inferring expansive systems.

In the case of **AB2**, we have

$$\hat{\lambda}h = \frac{2\zeta^2 - 2\zeta}{3\zeta - 1}.$$

When $a < 0$, $\text{Re}(\hat{\lambda})$ can be positive for $e^a < 1/3$ and $\theta \in (-\pi/2, \pi/2)$, leading to misinterpretation of decaying modes as growing. However, $\hat{\lambda}$ contains a negative real part for $a = 0$.

For the **BDF2** method, the expression is

$$\hat{\lambda}h = \frac{3 - 4\zeta + \zeta^2}{2\zeta^2}.$$

When $a < 0$, small values of $|\zeta|$ can lead to large positive values of $\text{Re}(\hat{\lambda}h)$. When $a = 0$, the sign of $\text{Re}(\hat{\lambda}h)$ varies with θ , making the method unpredictable for learning oscillatory modes.

The **AM2** method yields

$$\hat{\lambda}h = \frac{12\zeta^2 - 12\zeta}{5\zeta^2 + 8\zeta - 1}.$$

If $a < 0$, $\text{Re}(\hat{\lambda})$ can be positive for $a < -2.15$ and $\theta \in (-\pi/2, \pi/2)$, while $\text{Re}(\hat{\lambda})$ is always negative under the setting that $a = 0$. It is therefore robust for learning non-expansive dynamical systems.

For the **Leap-Frog** method, the effective parameter is

$$\hat{\lambda}h = \frac{\zeta^2 - 1}{2\zeta}, \quad \text{so that} \quad \text{Re}(\hat{\lambda}h) = \sinh(a) \cos(\theta).$$

This implies that when $a < 0$, the real part is negative if $\cos(\theta) > 0$, and positive otherwise. In the purely oscillatory case where $a = 0$, $\sinh(a) = 0$, therefore $\text{Re}(\hat{\lambda}h) = 0$.

Since the roots satisfy $\zeta_1\zeta_2 = -1$, one of the simple roots always lies outside the unit circle. An important consequence is that: *if one solves the learned dynamical system, $dz/dt = \hat{\lambda}z$, with other conditions, a perturbation of the perfect ones, one may obtain trajectories containing the spurious roots with growing amplitude.*

Phase errors in systems learned from Leap-Frog.

The Leap-Frog method exhibits markedly different behavior in how it encodes the phase of oscillatory dynamics. Suppose $|\theta|$ is small, $\text{Im}(\hat{\lambda}h)$ preserves the sign of $\sin(\theta) \approx \theta$. This means that the Leap-Frog method will infer rotation directions that are consistent with the actual system.

In the Leap-Frog method,

$$\hat{\lambda}h = \frac{\zeta^2 - 1}{2\zeta} \quad \Rightarrow \quad \text{Im}(\hat{\lambda}h) = \cosh(a) \sin \theta.$$

Notably, when $a = 0$, the method will infer a system without any phase error, while for $a < 0$, the rotational speed is reduced by the dissipation in the actual system.

Thus, Leap-Frog exhibits high phase fidelity but at the cost of stability, as it always includes one unstable root.

3.2 Conservative dynamics and higher order Adams methods

In this section, we analyze the systems learned from using the AB k and AM k methods for $k = 3$ and $k = 4$. In Figures 8 and 9, we summarize the systems learned from using these methods to fit $Z_n = e^{n\lambda h}$, where λ has both non-zero real and imaginary parts. From our observations, higher-order Adams methods tend to infer expansive systems; therefore, they seem not viable for learning systems with dissipa-

Table 3: Stable and unstable roots of two-step LMMs applied to $z' = \lambda z$.

| Method | Stable/unstable roots coexist ($ \zeta_1 \geq 1$ and $ \zeta_2 \leq 1$) | Repeated roots ($\zeta_1 = \zeta_2$) |
|-----------|--|--|
| AB2 | Dark Gray region in Figure 6a | if $\lambda h = \frac{-4 \pm 4\sqrt{4}i}{9}$, $ \zeta_{1,2} < 1$ |
| AM2 | Dark Gray region in Figure 6b | if $\lambda h = \frac{-6 \pm 4\sqrt{3}i}{7}$, $ \zeta_{1,2} > 1$ |
| BDF2 | Dark Gray region in Figure 6c | if $\lambda h = -\frac{1}{6}$, $ \zeta_{1,2} < 1$ |
| Leap-Frog | always, since $\zeta_1\zeta_2 = -1$ | if $\lambda h = \pm i$, $ \zeta_{1,2} = 1$ |

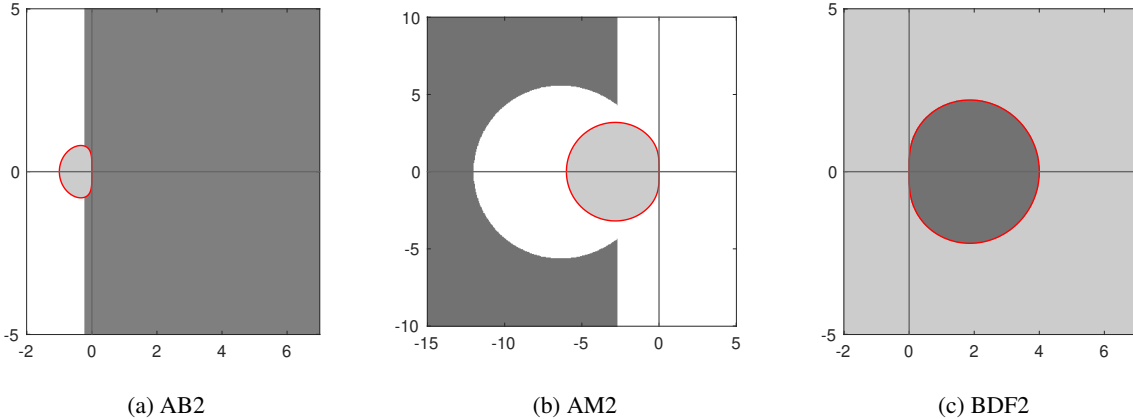


Figure 6: The dark gray region in each panel marks the set of complex numbers z where both characteristic roots satisfy $|\zeta_1(z)| \geq 1$ and $|\zeta_2(z)| \leq 1$. The regions in light gray are the region of absolute stability \mathcal{R}_A of each integrator, which is enclosed by the red curve.

tion. In this subsection, we analyze how these methods perform for learning purely oscillatory systems and summarize our findings in the following two corollaries.

Corollary 3.1 (Characterization of $\hat{\lambda}$ Learned by Adams–Bashforth Methods). *Assume that λh meets the Nyquist condition (2.1) and $h > 0$. Let $\hat{\lambda} h$ be a global minimizer of (25), with $m = 1$ and $Z_n = e^{n\lambda h}$, $n = 0, 1, \dots, N$, involving a k -step Adams–Bashforth method (AB k), where $k = 3, 4$. Then the following properties hold:*

Table 4: Sign of $\text{Re}(\hat{\lambda}h)$ for two-step methods, inferred from root $\zeta = e^{a+i\theta}$.

| Method | Data with damping ($a < 0$) $\text{Re}(\hat{\lambda}h) > 0$ | Pure oscillatory data ($a = 0$) $\text{Re}(\hat{\lambda}h) < 0$ for all $\zeta \in S^1$ |
|-----------|--|--|
| AB2 | Gray region in Figure 7a | $\text{Re}(\hat{\lambda}h) < 0$ for all $\zeta \in S^1$ |
| AM2 | Gray region in Figure 7b | $\text{Re}(\hat{\lambda}h) < 0$ for all $\zeta \in S^1$ |
| BDF2 | Gray region in Figure 7c | $\text{Re}(\hat{\lambda}h)$ can be positive |
| Leap-Frog | $\text{Re}(\hat{\lambda}h) > 0$ if $\cos(\theta) < 0$ $\text{sign}(\text{Im}(\hat{\lambda}h)) = \cosh(a) \sin \theta$ | $\text{Re}(\hat{\lambda}h) = 0$ for all $\zeta \in S^1$ small $ \theta \implies$ small phase error |

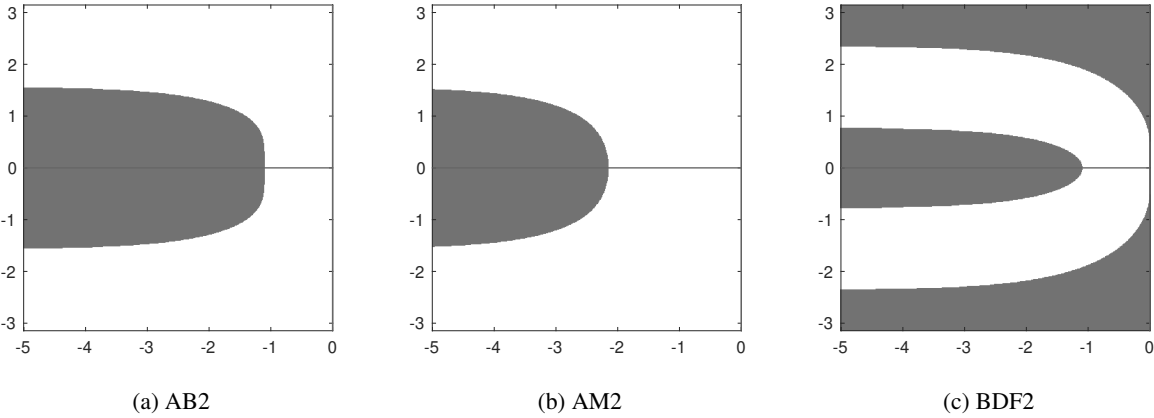


Figure 7: The dark gray region in each panel marks the set of complex numbers $z = a + i\theta$ where $\text{Re}(\hat{\lambda}h) = \text{Re}\left(\frac{\rho(e^z)}{\kappa(e^z)}\right) > 0$.

- *The imaginary part is preserved in sign:*

$$\text{sign}(\text{Im}(\hat{\lambda})) = \text{sign}(\text{Im}(\lambda)).$$

- *The real part behaves as follows:*

[AB3] $\text{Re}(\hat{\lambda}) < 0$ if $\cos(\text{Im}(\lambda h)) < \frac{1}{10}$; otherwise $\text{Re}(\hat{\lambda}) \geq 0$.

[AB4] $\text{Re}(\hat{\lambda}) < 0$ if $\cos(\text{Im}(\lambda h)) < -\frac{4}{9}$; otherwise $\text{Re}(\hat{\lambda}) \geq 0$.

Corollary 3.2 (Characterization of $\hat{\lambda}$ Learned by Adams–Moulton Methods). *Assume that λh meets the Nyquist condition (2.1) and $h > 0$. Let $\hat{\lambda}h$ be a global minimizer of (25), with $m = 1$ and $Z_n = e^{n\lambda h}$, $n = 0, 1, \dots, N$, involving a k -step*

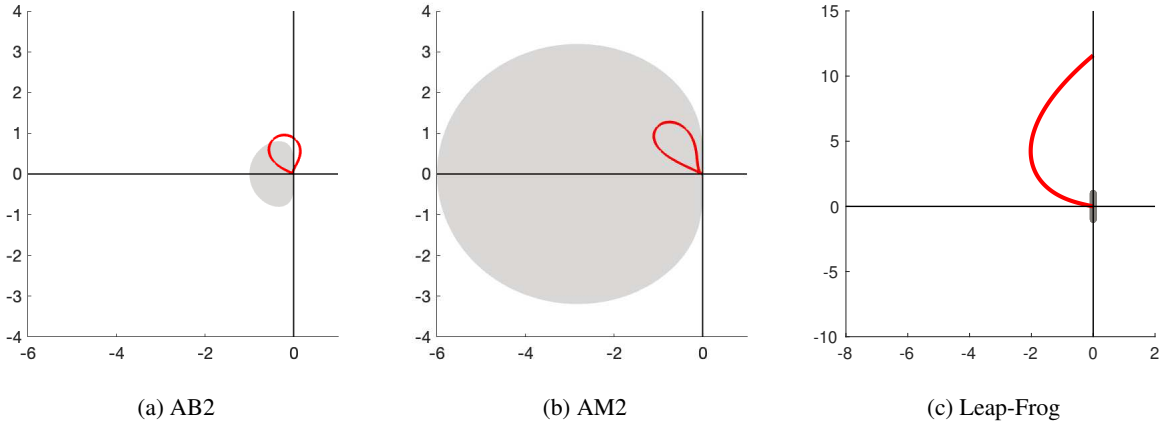


Figure 8: $\hat{\lambda}h$ versus the region of absolute stability. The gray region in each plot indicates the stability region of the selected method, while the red curve depicts the learning result, $\hat{\lambda}h = \rho(e^{\lambda h})/\kappa(e^{\lambda h})$ for $h \in (0, \pi/4)$, where $\lambda = -4 + 2i$.

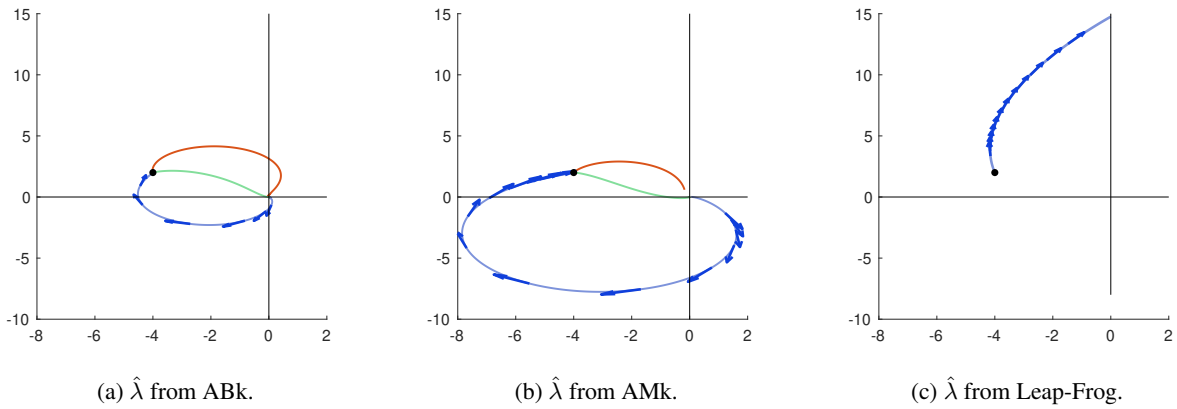


Figure 9: $\hat{\lambda} \equiv \hat{\lambda}(h) = h^{-1}\rho(e^{\lambda h})/\kappa(e^{\lambda h})$ for $h \in (0, \pi/4)$. The actual value, $\lambda = -4 + 2i$, is indicated by a triangle in each plot. The arrows on selected curves show the trend of $\hat{\lambda}$ as $h \rightarrow 0$ for the respective methods. The blue curves represent the ABk or AMk methods for $k = 2$, the green curves for $k = 3$, and the red curves for $k = 4$. The right plot corresponds to the Leap-Frog scheme.

Adams–Moulton method (AM k), where $k = 3, 4$. Then the following properties hold:

- *The imaginary part is preserved in sign:*

$$\text{sign}(\text{Im}(\hat{\lambda})) = \text{sign}(\text{Im}(\lambda)).$$

- *The real part behaves as follows:*

$$[\text{AM3}] \text{Re}(\hat{\lambda}) < 0.$$

[AM4] $\text{Re}(\hat{\lambda}) < 0$ if $\cos(\text{Im}(\lambda h)) < \frac{11}{38}$; otherwise $\text{Re}(\hat{\lambda}) \geq 0$.

According to Lemma 3.1, the learned dynamic resides on the boundary of each method's stability region. In particular, the Leap-Frog scheme is absolutely stable in the interval $(-1, 1)$, the imaginary axis. Consequently, the learned dynamical system, $dz/dt = \hat{\lambda}z$, will be conservative if the data points come from a conservative dynamical system, and $0 \leq |\hat{\lambda}| < 1/h$, for any step size h . This implies that the frequency in the learned dynamical system has to be smaller than the actual frequency. In contrast, the stability regions of the Adams-family methods intersect the imaginary axis at a finite number of points; some even extend to the right half of the complex plane. Consequently, the learned dynamics will typically exhibit dissipative behavior if the stability region stays on the left half-plane, and may even be expansive when the stability region overlaps the right half-plane. Our analysis suggests that the Leap-Frog scheme is better suited for learning conservative dynamics within the LMM framework.

3.3 Noisy data

We study the dynamics inferred by the Leap–Frog and noisy observations. The point is that the presence of noise in data observed from a dissipative system may result in the learned discrete dynamical system becoming unstable. The instability is caused by the existence of spurious roots of the corresponding characteristic polynomial.

For a learned parameter λ^*h , the Leap–Frog solution at n step can be written as

$$c_1\zeta_1^n + c_2\zeta_2^n, \quad \zeta_{1,2} := \lambda^*h \pm \sqrt{1 + (\lambda^*h)^2},$$

with coefficients c_1, c_2 determined by the initial values z_0 and z_1 .

Theorem 3.2 (Admissible region for λ^*h). *Let N be sufficiently large and let λ^*h be the global minimiser of (26) obtained with the Leap–Frog scheme. Suppose the observations*

$$e^{\lambda n h} + \epsilon_n, \quad n = 1, \dots, N,$$

are uniformly bounded and include zero-mean noise ϵ_n of small variance, where $\text{Re}(\lambda) < 0$ and h is the sampling step.

Assume that

$$|\zeta_1| > 1, \quad |\zeta_2| \leq 1.$$

Then we must have

$$c_1 = 0, \quad \lambda^*h \in \{z \in \mathbb{C} : \text{Re}(z) < 0\} \cup [-i, i].$$

Proof. Assume that both coefficients are non-zero, $c_1 \neq 0$ and $c_2 \neq 0$. By the triangle inequality,

$$|c_1\zeta_1^n + c_2\zeta_2^n - e^{\lambda nh} + \epsilon_n| \geq \left| |c_1||\zeta_1|^n - |c_2\zeta_2^n + e^{\lambda nh}| - |\epsilon_n| \right|.$$

Because $|c_2\zeta_2^n + e^{\lambda nh}|$ is uniformly bounded, $|\epsilon_n|$ is small, and $|\zeta_1| > 1$, the right-hand side grows without bound as $n \rightarrow \infty$. Hence, the residual cannot be minimized globally, contradicting the optimality of λ^*h . Therefore, we must have $c_1 = 0$.

With $c_1 = 0$, the Leap–Frog solution reduces to $c_2\zeta_2^n$, and stability requires $|\zeta_2| \leq 1$, i.e.

$$|\lambda^*h - \sqrt{1 + (\lambda^*h)^2}| \leq 1.$$

A straightforward calculation shows that this inequality holds precisely when either

$$\operatorname{Re}(\lambda^*h) < 0 \quad \text{or} \quad \lambda^*h \in [-i, i].$$

□

An example of “hidden” spurious mode

Due to the presence of noise in the data, the coefficient c_1 for the spurious root does not necessarily vanish. To illustrate this fact, we estimate λ^*h from synthetic observations $Z_n = Z_0e^{\lambda nh} + \epsilon_n$ generated from the linear system with $\lambda = -3 + i$ with the sampling step size $h = 0.1$ and the starting point Z_0 ; here ϵ_n is the noise with zero mean and variance 0.01, $n = 1 \cdots N = 10$. In Table 5 we report the resulting c_1 and c_2 values for several choices of N .

If the coefficient, c_1 , linked to the spurious root is non-zero, the learned discrete dynamics can diverge from the actual system at later times. To show this, we use snapshots at $t_n = nh$, $n = 0, \dots, 10$, to estimate λ^* and the coefficients c_1, c_2 . Then we integrate this learned system up to $t = 5$. Figure 10 shows that, in such a case, the spurious root eventually dominates, and the numerical solution eventually diverges.

Table 5: Estimated coefficients c_1 and c_2 for different sample sizes N .

| N | c_1 | c_2 | $ \zeta_1 $ | $ \zeta_2 $ |
|-----|-------------------------|--------|-------------|-------------|
| 10 | -5.086×10^{-6} | 1.0019 | 1.8376 | 0.7455 |
| 20 | -1.952×10^{-7} | 1.0005 | 1.6337 | 0.7448 |
| 50 | 1.135×10^{-10} | 1.0003 | 1.3499 | 0.7456 |

Besides, we further analyze how the learned dynamic $\hat{\lambda}h$ —obtained from noise-free data—deviates from the dynamic λ^*h derived from noisy data.

Theorem 3.3. *Fix a step size $h > 0$. Let $\hat{\lambda}h$ be a global minimizer of the noise-free learning problem (25), and let λ^*h solve the noisy setting*

$$\begin{aligned} \min_{\xi \in \mathbb{C}} \quad & L(\xi) := \frac{1}{N} \sum_{k=1}^N |z_k - (e^{\lambda h k} Z_0 + \epsilon_k)|^2 \\ \text{s.t.} \quad & z_{n+2} = z_n + 2\xi z_{n+1}, \\ & z_0 = Z_0 + \epsilon_0, \quad z_1 = Z_0 e^{\lambda h} + \epsilon_1, \end{aligned}$$

where Z_0 is a complex number, and the noises satisfy $|\epsilon_k| \leq \sigma$. Introduce functions f_n, g_n such that we can write $z_{n+2} = f_n(\xi h)z_0 + g_n(\xi h)z_1$. Assume

1. $|\lambda^*h| \leq M$;

2. for every $\theta \in [0, 1]$ and $\eta = \theta \hat{\lambda} + (1 - \theta)\lambda^*$,

$$|f'_n(\eta h)|, |g'_n(\eta h)| \geq c_0 > 0,$$

with c_0 independent of k and σ .

Then there exists a constant $C = C(Z_0, M, c_0)$ such that

$$|\lambda^*h - \hat{\lambda}h|^2 \leq C \sigma^2 = \mathcal{O}(\sigma^2).$$

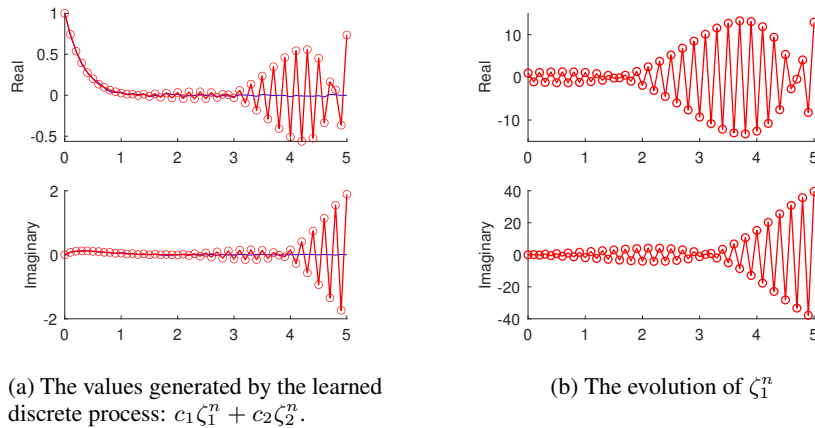


Figure 10: The x-axis represents the physical time. The blue curves represent the observed data. On the left, the red curves depict the numerical solution of the differential equation $z' = \lambda^*z(t)$ obtained using the Leap-Frog scheme with step size $h = 0.1$ up to time $t = 5$. On the right, the plots display the evolution of ζ_1^n .

4 Numerical experiments

This section presents some further numerical studies to verify and further illustrate our findings on non-negligible numerical effects that lead to mistakenly inferring unstable systems, destruction of orbits, or limiting cycles, and oscillatory systems with large nonlinear phase errors.

Some of the examples below involve comparisons using the Implicit Trapezoidal Rule and the Implicit Midpoint Rule; these two methods coincide with each other for linear systems. Here, for clarity, we provide their generic forms for nonlinear autonomous systems $y' = f(y)$:

$$y_{n+1} = y_n + h f\left(\frac{y_n + y_{n+1}}{2}\right), \quad (\text{Implicit Midpoint Rule})$$

$$y_{n+1} = y_n + \frac{h}{2} (f(y_n) + f(y_{n+1})). \quad (\text{Implicit Trapezoidal Rule})$$

4.1 Noisy data from a harmonic oscillator

We analyze the relationship between noise levels and the differences in learning results from noise-free and noisy data by considering the harmonic oscillator,

$$\mathbf{x}'(t) = \begin{pmatrix} 0 & \lambda \\ -\lambda & 0 \end{pmatrix} \mathbf{x}(t), \quad \mathbf{x}(0) = \begin{pmatrix} 1 \\ 0 \end{pmatrix}. \quad (31)$$

The learning goal is to recover the matrix A in the linear system $\mathbf{x}' = A\mathbf{x}$ that best fits the observation data.

We fix $\lambda = 1$ and use a sampling step $h = 1/128$. Let A^* be the matrix learned from noise-free data, and \hat{A} the matrix obtained when the observations are perturbed with additive noise $\epsilon_n \sim \mathcal{N}(0, \sigma I)$.

For each noise level, we repeat the training 10 times, compute $\|A^* - \hat{A}\|_2$ for each run, and report their empirical mean and variance.

Figure 11 confirms Theorem 2.5 and Theorem 3.3 that the difference between the noisy-data estimate A^* and the reference matrix \hat{A} has a first-order dependence on the noise level.

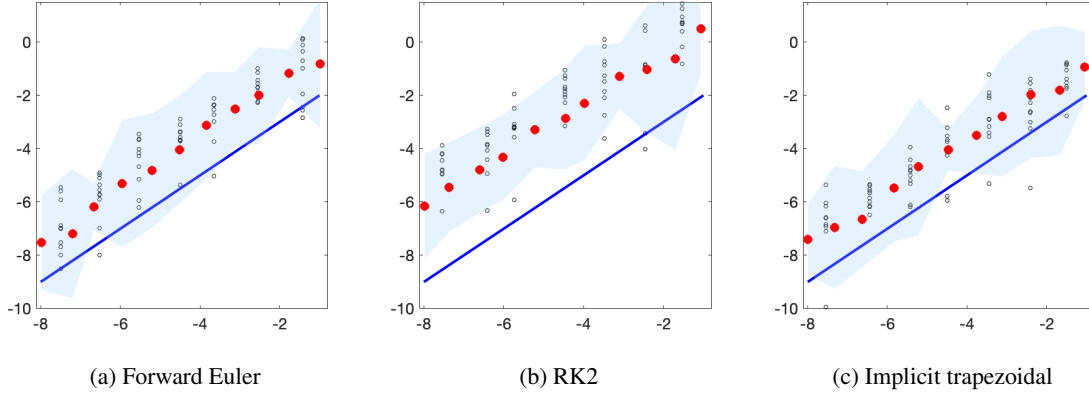


Figure 11: Log-log plots (base 2) of $\|A^* - \hat{A}\|_2$ versus the noise level σ . The open circles mark results of each trial, and the filled circles show their means, while the light-blue shaded ribbon encloses ± 3 standard deviations of the estimates. The blue line labels the slope as 1 for reference to visualize the relationship between the noise level and $\|A^* - \hat{A}\|_2$.

4.2 Recovering coefficients in a convection-diffusion equation

In this example, we consider the recovery of the coefficients a and ϵ in the following convection-diffusion equation with the periodic boundary condition,

$$\begin{aligned} u_t &= au_x + \epsilon u_{xx}, \quad x \in [0, 1), t \in \mathbb{R}^+, \\ u(x, t = 0) &= u_0(x), \end{aligned} \quad (32)$$

with $a = 2$ and $\epsilon = 0.01$.

We consider the spectral method and use data u_j^n on a Cartesian grid, with $x_j = j\Delta x$, $j = 0, 1, 2, \dots, 256$, and $t_n = nh$, for $n = 1, 2, \dots, 5 \times 10^4$. The data are computed by the Matlab's ODE45 with $\text{AbsTol} = 10^{-12}$ and $\text{RelTol} = 10^{-12}$.

We denote the optimal coefficients by \hat{a} and $\hat{\epsilon}$. In Table 6, we compare the values of \hat{a} and $\hat{\epsilon}$ obtained by using Forward Euler, Backward Euler, and Implicit Trapezoidal Rule, and with the data from two different initial values

$$u_0(x) = \cos(2\pi kx), \quad k = 1, 10.$$

This example verifies Theorem 2.1 and Corollary 2.1, and Corollary 2.3. In particular, the stability of the Backward Euler on the right complex plane can lead to identifying a diffusion coefficient with the wrong sign!

From Table 6, we also see that \hat{a} is strictly smaller than a for the Forward Euler method. In contrast, the values of \hat{a} estimated from the Backward Euler method are larger than a . These results can be explained by our analysis in Section 2.

Table 6: The learned coefficients \hat{a} and $\hat{\epsilon}$ for (32) using different time stepping schemes. The true values are $a = 2$ and $\epsilon = 0.01$.

| Forward Euler | $k = 1$ | | $k = 10$ | |
|---------------|-----------|------------------|-----------|------------------|
| | \hat{a} | $\hat{\epsilon}$ | \hat{a} | $\hat{\epsilon}$ |
| $h = 10^{-2}$ | 1.9869 | 0.0299 | 1.0281 | 0.0199 |
| $h = 10^{-3}$ | 1.9992 | 0.0120 | 1.9181 | 0.0117 |

| Backward Euler | $k = 1$ | | $k = 10$ | |
|----------------|-----------|------------------|-----------|------------------|
| | \hat{a} | $\hat{\epsilon}$ | \hat{a} | $\hat{\epsilon}$ |
| $h = 10^{-2}$ | 2.0026 | -0.0100 | 2.2552 | -0.0133 |
| $h = 10^{-3}$ | 2.0007 | 0.0080 | 2.0748 | 0.0081 |

| Implicit Trap. | $k = 1$ | | $k = 10$ | |
|----------------|-----------|------------------|-----------|------------------|
| | \hat{a} | $\hat{\epsilon}$ | \hat{a} | $\hat{\epsilon}$ |
| $h = 10^{-2}$ | 2.0026 | 0.0100 | 2.1765 | 0.0146 |
| $h = 10^{-3}$ | 2.0000 | 0.0100 | 2.0018 | 0.0100 |

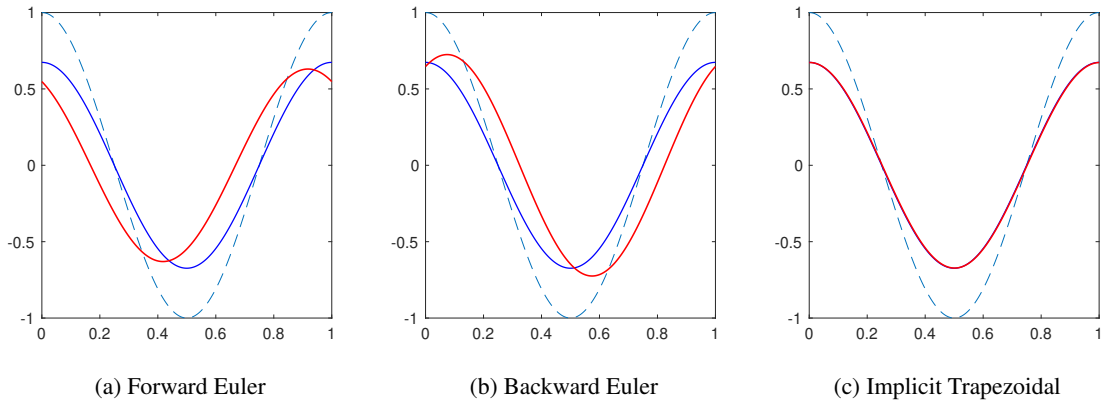


Figure 12: Profiles of the learned convection–diffusion solution at $T = 1$. The blue dashed line denotes the initial condition $\cos(2\pi x)$, the solid blue line is the true solution, and the red line represents the learned solution.

Note that the imaginary part of the solution to (32) is directly associated with the propagation speed a in the governing equation. To emphasize the distortion in the imaginary component between the learned and true dynamics, we plot the solution and analyze its propagation behavior. Specifically, we simulate the solution with the initial condition $u_0 = \cos(2\pi x)$, using the coefficients learned with $k = 10$ and $h = 10^{-3}$, as reported in Table 6. Figure 12 supports the conclusion in Table 2, showing that the Forward Euler method learns a dynamic with a slower propagation speed, whereas the Backward Euler method, by contrast, learns a dynamic with an advanced propagation speed.

4.3 Neural ODE models for the Lotka-Volterra system

We study the learning of orbital trajectories in a nonlinear predator-prey problem, using a common Neural ODE approach.

The Lotka-Volterra dynamic describes the interaction between two species,

$$\begin{cases} \frac{dx}{dt} = x \left(1 - \frac{y}{\nu}\right), \\ \frac{dy}{dt} = \frac{y}{\nu} (1 - x), \end{cases}$$

where $\nu > 0$. We will construct, from data, neural networks to approximate the vector field of this system (the right-hand side of the above equation).

We set $\nu = 1$ in this study, and generate trajectories by integrating the dynamic system using MATLAB's ODE45 solver and setting `AbsTol` and `RelTol` to 10^{-12} . We sample trajectory snapshots at $t_n = nh$ with $h = 10^{-1}, 10^{-2}$, and $0 \leq t_n \leq 12$. That is, training dataset \mathcal{D}_h is sampled over the time interval $[0, 12]$ with timesteps $h = 10^{-1}$ and 10^{-2} . The trajectories of the learned dynamics are generated using the 4th-order Runge-Kutta method over the time interval $[0, 40]$ with $\Delta t = 10^{-4}$.

The neural networks are simple multilayer perceptrons consisting of three hidden layers, each with 100 nodes, and utilize the ELU function as their activation function. We stop the training after the mean squared error between the prediction and training data reaches 10^{-4} . When applied to the system linearized around an orbit, the theory developed in the previous sections can be used to understand the local behavior of the nearby trajectories:

- The Backward Euler may lead to expansive systems, a consequence corresponding to the possibility that $\text{Re}(\hat{\lambda}) > 0$;

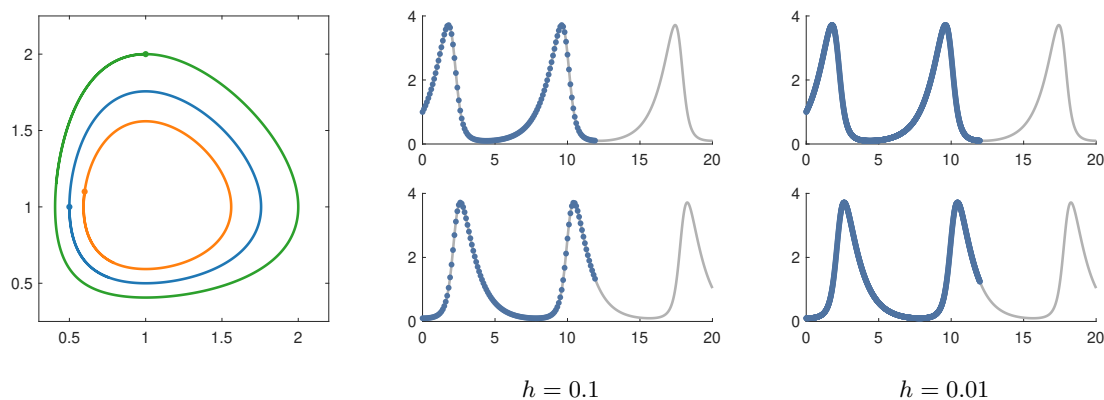


Figure 13: Three Lotka–Volterra orbits are displayed. Filled circles mark samples from the blue orbit. In the time-series panels, the horizontal axis is time; the upper panel plots the x -information and the lower panel plots the y -information of the sampled points.

- The Implicit Trapezoidal Rule and Implicit Midpoint Rule (these two methods coincide for linear problems) can better capture the nonlinear conservative nature of the dynamical system; a consequence corresponding to the method’s stability region includes the imaginary axis but not the right half plane.
- The observed orbits may become a limit cycle for the vector field learned by the Implicit Trapezoidal and Implicit Midpoint Rules.

See the top row in Figure 14. Additionally, the second row shows trajectories originating from various initial data points. Although the Implicit Trapezoidal Rule and the Implicit Midpoint Rule more effectively capture the conservative property of the training data, the other trajectories, e.g., the orange and green trajectories, do not generate a close orbit. The orbit where the observation snapshots lie seems to be a limit cycle for the learned vector field. Observe that both the orange and the green trajectories spiral towards the purple.

Figure 14 presents the learned dynamics trained using data sampled from $h = 0.1$. Even though the data points “cover” a wider region, the undesirable numerical artifacts from the Backward Euler method persist.

Figure 15 shows the learning results using the dataset with $h = 0.01$. Although a finer sampling timestep is used, the learning results using the Backward Euler method continue to show expansive outcomes.

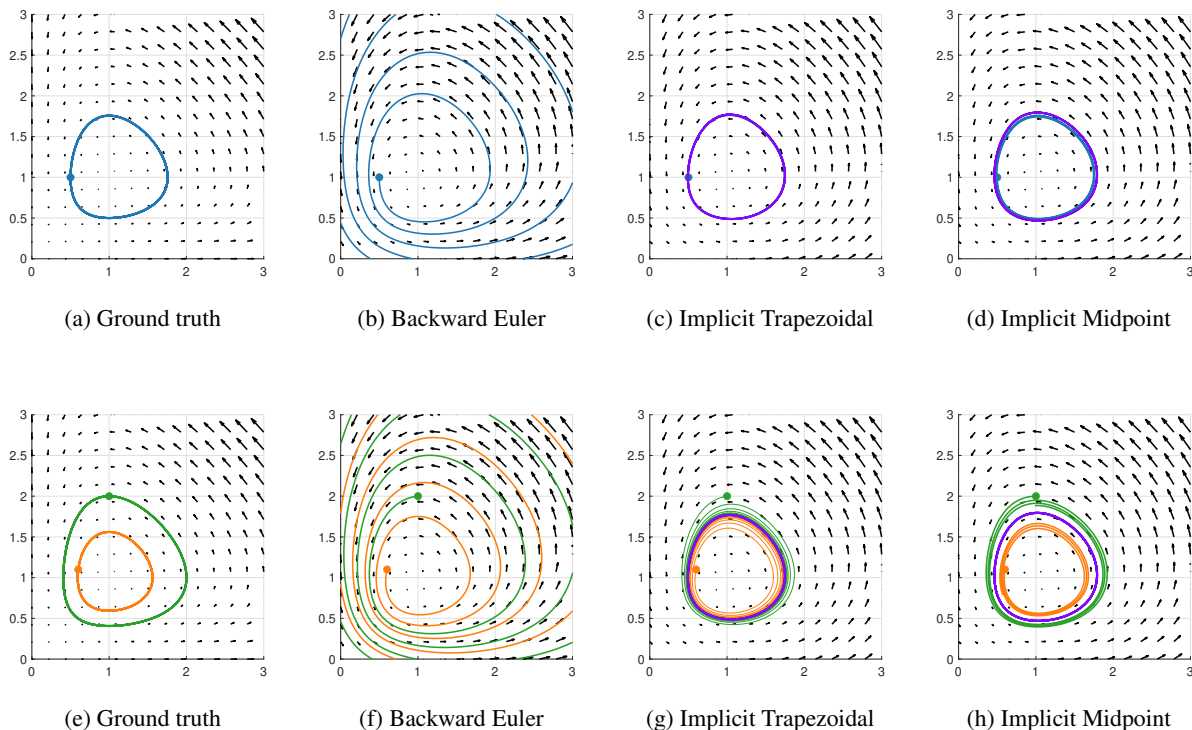


Figure 14: Learning results with timestep $h = 0.1$ using the Backward Euler, implicit trapezoidal, and implicit midpoint methods. The top row presents trajectories generated by the learned dynamics from initial conditions within the training set, while the bottom row shows trajectories from initial conditions outside the training set. The purple orbits in (c), (d), (g), and (h) seem to become limiting cycles.

4.4 Neural ODE models for a relaxation oscillator

In this example, we will study the stability properties of learned Neural ODE models constructed with data from a trajectory of the following nonlinear oscillator [1] [7]:

$$\begin{cases} \frac{dx}{dt} = -1 - x + 8y^3, \\ \frac{dy}{dt} = \frac{1}{\nu}(-x + y - y^3). \end{cases}$$

For $0 < \nu \ll 1$, the trajectories of this system will converge to a limiting cycle defined by $x = y - y^3$; see Figure 16.

We show below that our linear theories can explain why a learned system may not follow the structure (limiting cycle) in the training data.

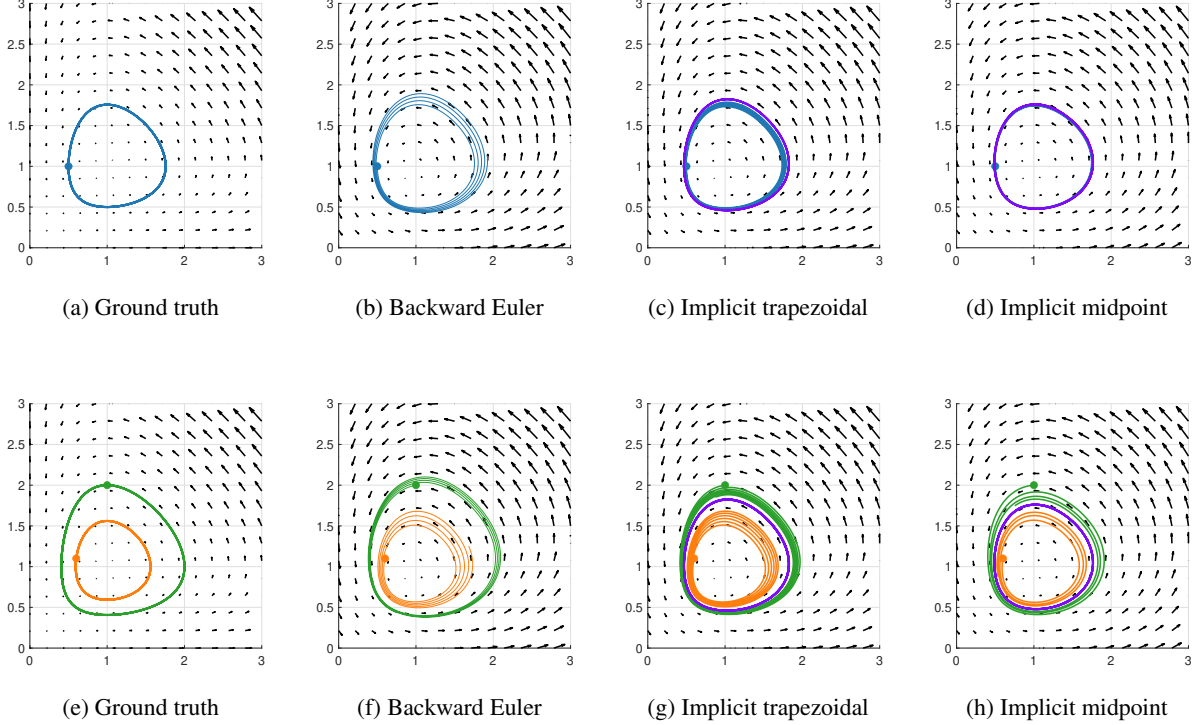


Figure 15: Learning results with timestep $h = 0.01$ using the Backward Euler and implicit trapezoidal and implicit midpoint methods. The top row presents trajectories generated by the learned dynamics from an initial condition within the training set. In contrast, the bottom row shows trajectories from initial conditions outside the training set.

We train simple multilayer perceptrons, denoted as g_h , to approximate the vector field, $f(x, y)$, so that a flow line of $g_h(x, y)$ fits the observed trajectory well. The network architecture consists of three hidden layers, each containing 100 nodes, and utilizes the ELU() activation function. We terminate the training when the loss function falls below 10^{-4} .

We set $\nu = 0.1$ in this study, and generate trajectories by integrating the dynamic system using MATLAB's ODE45 solver and setting `AbsTol` and `RelTol` to 10^{-12} . We sample trajectory snapshots at $t_n = nh$ with $h = 10^{-1}, 10^{-2}$, and $0 \leq t_n \leq 5$. As in other parts of this paper, the subscript h in g_h reflects the step size used during training by the Forward Euler method to integrate the vector field $g_h(x, y)$.

For convenience, we denote the solution of this system by $\gamma(t; \gamma_0) = (x(t), y(t))$ with $\gamma_0 := (x(0), y(0))$. We use $f(\gamma) \equiv f(x, y)$ to denote the right-hand-side of the ODE, and $g_h(x, y)$ to denote a neural network trained to fit the given trajectory data.

Denote $\lambda := \lambda(\gamma)$ and $\hat{\lambda} := \hat{\lambda}(\gamma)$ an eigenvalue of the Jacobian, $J_f(\gamma)$, and $J_{g_h}(\gamma)$ at γ respectively.

From this example, our studies show that

- As predicted by our theory, the Jacobian eigenvalues of the learned dynamics fall within the stability region of the Forward Euler method, see Figure 17;
- Furthermore, due to the presence of non-trivial imaginary part in $\lambda(\gamma)$, and the shape of Forward Euler’s stability region, the learned dynamics could have a larger dissipation; i.e. $\text{Re}(\hat{\lambda}) < \text{Re}(\lambda)$; Figure 18;
- Consequently, the trajectories from g_h may not converge to a limiting cycle close to the ground truth. See Figure 20.

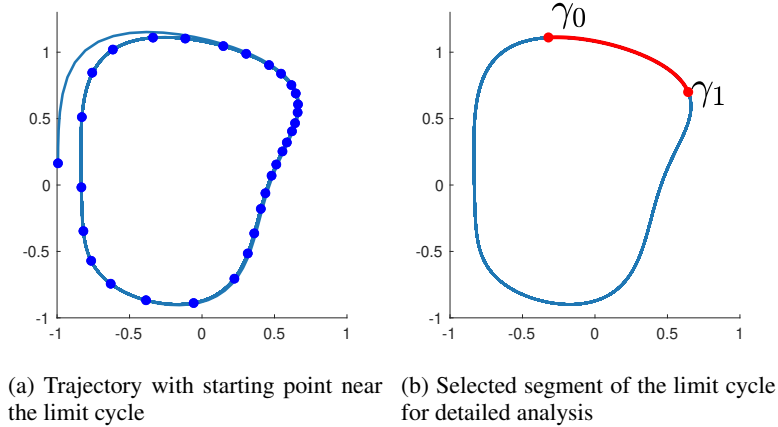


Figure 16: The left panel shows the trajectory where data is sampled, which also encompasses a limit cycle. The right panel highlights the segment chosen for detailed analysis.

4.5 Neural ODE models for a damped nonlinear pendulum

We come back to study the nonlinear pendulum mentioned in the Introduction. Even though the sampling rate is significantly higher than the Nyquist rate, we shall observe the striking differences in the *amplitudes and phases of oscillations* in the fully resolved trajectories of the learned neural ODE models.

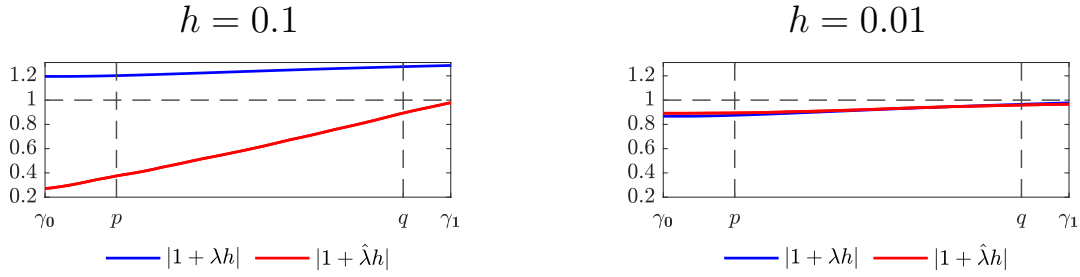


Figure 17: Profiles of $|1 + \lambda(x)h|$ and $|1 + \hat{\lambda}(x)h|$ along the upper branch of the limit cycle.

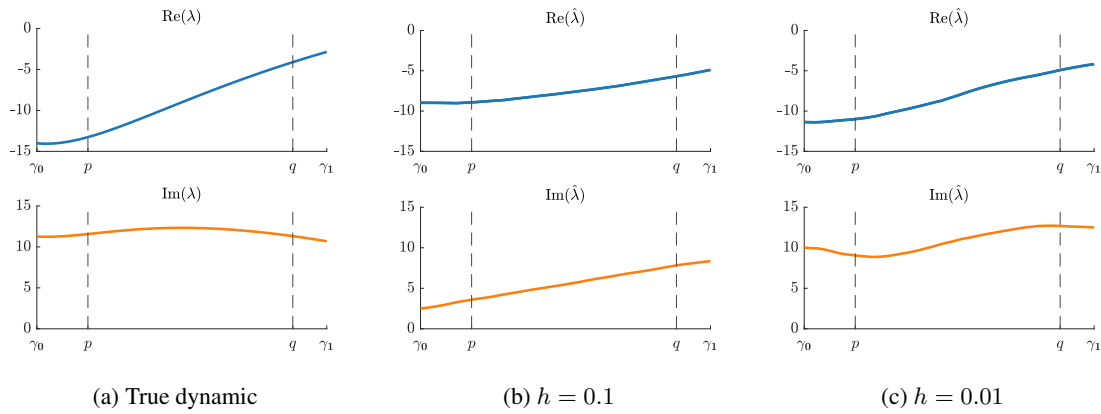


Figure 18: Real and imaginary components of the Jacobian eigenvalues for both the learned and true dynamics along the sampled branch; the x-axis ticks match the labels in Figure 16.

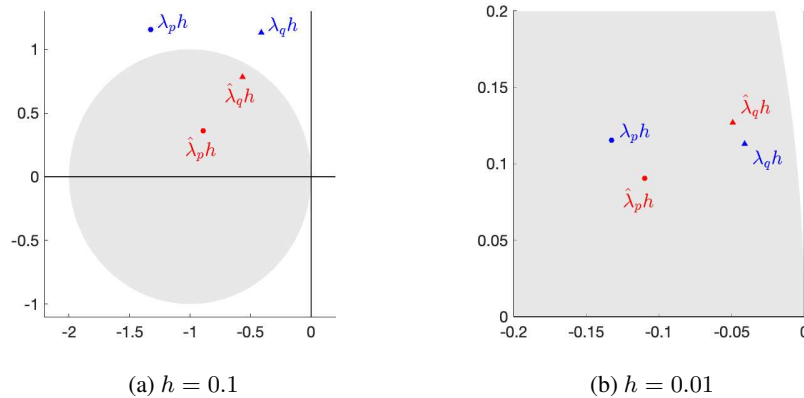


Figure 19: Comparison of the eigenvalues λ and $\hat{\lambda}$ of J_f and J_{g_h} at points p and q . The eigenvalues are scaled by the step size used by the numerical integrator and plotted on the complex plane, with the gray regions indicating the integrator's stability region.

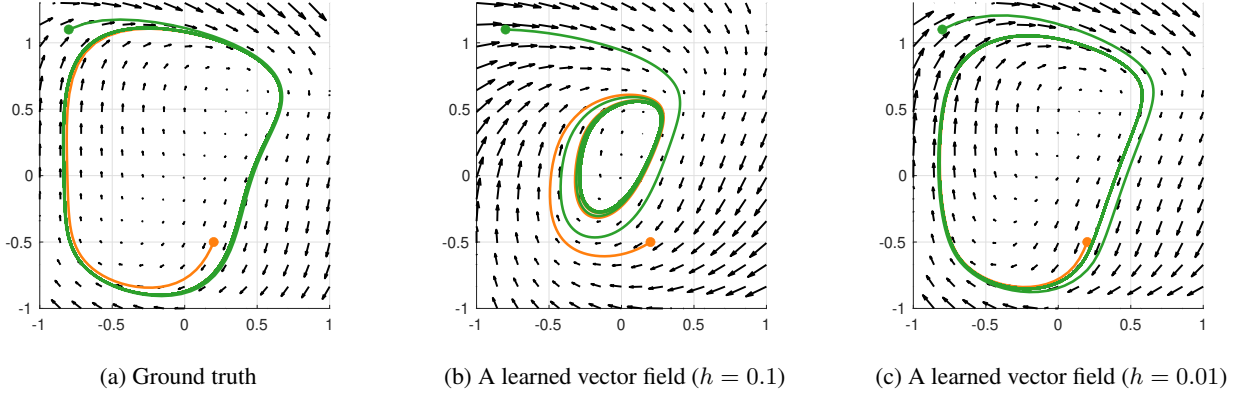


Figure 20: Vector fields using only one trajectory with different sampling timesteps.

We use the damped pendulum governed by

$$\begin{cases} \frac{d\vartheta}{dt} = \omega, \\ \frac{d\omega}{dt} = -\gamma\omega - \frac{g}{L}\sin\vartheta, \end{cases}$$

where we set $\gamma = 0.02$, $\frac{g}{L} = 9.81$. We simulate the trajectories of x and y using MATLAB's ODE45 solver and setting `AbsTol` and `RelTol` to 10^{-12} for $t \in [0, 40]$. Training snapshots are taken at $t_n = nh$ with $h = 10^{-1}$, and $0 \leq t_n \leq 10$.

The neural network is designed with three hidden layers and 100 neurons in each layer, and cooperating with the ELU activation function.

In Figure 21, we show the numerical artifacts of four numerical integrators used to learn the damped nonlinear pendulum system. We observe that The Backward Euler method infers a system that supports oscillations of much larger amplitudes; in contrast, the Forward Euler method infers a system with much larger damping. According to our theory, such discrepancies originate from the differences in the geometries of the stability regions of the integrators. We see that the Implicit Mid-point rule yields the most accurate learning, both in terms of amplitude and phase accuracy.

5 Conclusion

This article studies the potential non-negligible numerical artifacts in learning dynamical systems from observed trajectories. The choice of numerical integrator and

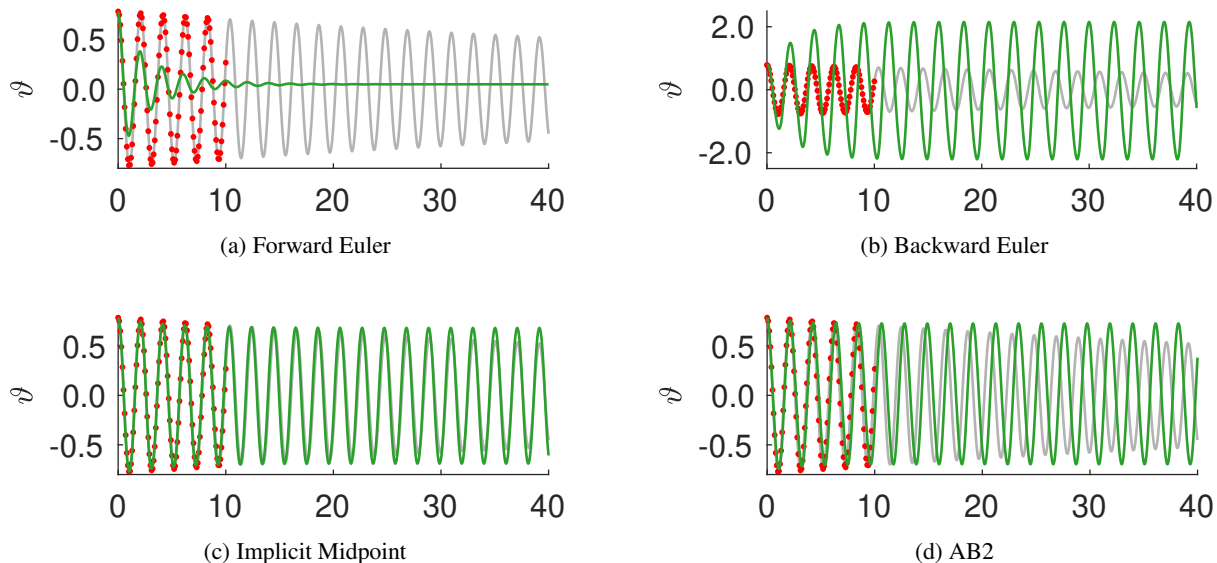


Figure 21: Amplitude errors of the learned solution component ϑ (green curves) inferred from applying four different numerical integrators to fit the data (red dots): (a) Forward Euler, (b) Backward Euler, (c) Implicit Midpoint, and (d) AB2. For reference, the true solution are shown by the gray curves.

its step size play a critical role. Interestingly, the stability of a numerical integrator does not even guarantee the stability of the learned dynamical system. What matters is the geometry of the integrator’s stability region on the complex plane. The superior stability of the Backward Euler method actually makes it the worse choice for forward computation in the type of inverse problems we considered in this paper. Assuming the sampling step size is selected to capture data over a full period of the actual dynamics, we observe that in one-step methods, only the implicit trapezoidal method accurately preserves both the amplitude and rotation direction, regardless of whether the actual dynamics are conservative or dissipative. Furthermore, we find that Richardson extrapolation may be used to consistently improve the accuracy of learning if the Implicit Midpoint Rule or the Implicit Trapezoidal Rule is involved. We also presented numerical studies demonstrating that our analysis can provide a way to analyze the learning problems for more complex nonlinear systems.

Acknowledgement

The authors thank Ufuk Topcu and Cyrus Neary for motivating conversations.

The first author thanks the Oden Institute for Computational Engineering and Sciences for hosting his visit.

The second author is supported partially by National Science Foundation grants DMS-2208504, DMS-2513857, and Army Research Office Grant W911NF2320240. Bing-Ze Lu received support from the National Science and Technology Council, Taiwan, through Grant 113-2917-I-564-033.

References

- [1] G. Ariel, B. Engquist, H.-O. Kreiss, and R. Tsai. Multiscale computations for highly oscillatory problems. In *Multiscale modeling and simulation in science*, pages 237–287. Springer Berlin Heidelberg Berlin, Heidelberg, 2009.
- [2] T. Bertalan, F. Dietrich, I. Mezić, and I. G. Kevrekidis. On learning hamiltonian systems from data. *Chaos: An Interdisciplinary Journal of Nonlinear Science*, 29(12), 2019.
- [3] S. L. Brunton, J. L. Proctor, and J. N. Kutz. Discovering governing equations from data by sparse identification of nonlinear dynamical systems. *Proceedings of the national academy of sciences*, 113(15):3932–3937, 2016.
- [4] M. Calvo, A. Murua, and J. Sanz-Serna. Modified equations for odes. *Contemporary Mathematics*, 172:63–63, 1994.
- [5] R. T. Chen, Y. Rubanova, J. Bettencourt, and D. K. Duvenaud. Neural ordinary differential equations. *Advances in neural information processing systems*, 31, 2018.
- [6] Z. Chen, J. Zhang, M. Arjovsky, and L. Bottou. Symplectic recurrent neural networks. *arXiv preprint arXiv:1909.13334*, 2019.
- [7] G. Dahlquist, L. Edsberg, G. Skölleremo, and G. Söderlind. Are the numerical methods and software satisfactory for chemical kinetics? In *Numerical Integration of Differential Equations and Large Linear Systems: Proceedings of two Workshops Held at the University of Bielefeld Spring 1980*, pages 149–164. Springer, 1982.
- [8] F. Djeumou, C. Neary, E. Goubault, S. Putot, and U. Topcu. Neural networks with physics-informed architectures and constraints for dynamical systems modeling. In *Learning for Dynamics and Control Conference*, pages 263–277. PMLR, 2022.

- [9] F. Djeumou, C. Neary, and U. Topcu. How to learn and generalize from three minutes of data: Physics-constrained and uncertainty-aware neural stochastic differential equations. *arXiv preprint arXiv:2306.06335*, 2023.
- [10] Q. Du, Y. Gu, H. Yang, and C. Zhou. The discovery of dynamics via linear multistep methods and deep learning: error estimation. *SIAM Journal on Numerical Analysis*, 60(4):2014–2045, 2022.
- [11] S. Greydanus, M. Dzamba, and J. Yosinski. Hamiltonian neural networks. In H. Wallach, H. Larochelle, A. Beygelzimer, F. d'Alché-Buc, E. Fox, and R. Garnett, editors, *Advances in Neural Information Processing Systems*, volume 32. Curran Associates, Inc., 2019.
- [12] M. Hersch, F. Guenter, S. Calinon, and A. Billard. Dynamical system modulation for robot learning via kinesthetic demonstrations. *IEEE Transactions on Robotics*, 24:1463–1467, 01 2008.
- [13] L. S. T. Ho, H. Schaeffer, G. Tran, and R. Ward. Recovery guarantees for polynomial coefficients from weakly dependent data with outliers. *Journal of Approximation Theory*, 259:105472, 2020.
- [14] P. Hu, W. Yang, Y. Zhu, and L. Hong. Revealing hidden dynamics from time-series data by odenet. *Journal of Computational Physics*, 461:111203, 2022.
- [15] R. T. Keller and Q. Du. Discovery of dynamics using linear multistep methods. *SIAM Journal on Numerical Analysis*, 59(1):429–455, 2021.
- [16] J. Z. Kolter and G. Manek. Learning stable deep dynamics models. In H. Wallach, H. Larochelle, A. Beygelzimer, F. d'Alché-Buc, E. Fox, and R. Garnett, editors, *Advances in Neural Information Processing Systems*, volume 32. Curran Associates, Inc., 2019.
- [17] B. O. Koopman. Hamiltonian systems and transformation in hilbert space. *Proceedings of the National Academy of Sciences*, 17(5):315–318, 1931.
- [18] M. Laurie and J. Lu. Explainable deep learning for tumor dynamic modeling and overall survival prediction using neural-ode. *npj Systems Biology and Applications*, 9(1):58, 2023.
- [19] J. Levinson, J. Askeland, J. Becker, J. Dolson, D. Held, S. Kammel, J. Z. Kolter, D. Langer, O. Pink, V. Pratt, et al. Towards fully autonomous driving: Systems and algorithms. In *2011 IEEE intelligent vehicles symposium (IV)*, pages 163–168. IEEE, 2011.

- [20] J. Lu, K. Deng, X. Zhang, G. Liu, and Y. Guan. Neural-ode for pharmacokinetics modeling and its advantage to alternative machine learning models in predicting new dosing regimens. *Iscience*, 24(7), 2021.
- [21] H. Lucas and R. Kelley. Generating control policies for autonomous vehicles using neural odes. In *ICLR 2020 Workshop on Integration of Deep Neural Models and Differential Equations*, 2019.
- [22] A. Mardt, L. Pasquali, H. Wu, and F. Noé. Vampnets for deep learning of molecular kinetics. *Nature communications*, 9(1):5, 2018.
- [23] I. Mezić. Spectral properties of dynamical systems, model reduction and decompositions. *Nonlinear Dynamics*, 41:309–325, 2005.
- [24] I. Mezić and A. Banaszuk. Comparison of systems with complex behavior. *Physica D: Nonlinear Phenomena*, 197(1-2):101–133, 2004.
- [25] C. Neary and U. Topcu. Compositional learning of dynamical system models using port-hamiltonian neural networks. In *Learning for Dynamics and Control Conference*, pages 679–691. PMLR, 2023.
- [26] Y. Oussar and G. Dreyfus. How to be a gray box: dynamic semi-physical modeling. *Neural networks*, 14(9):1161–1172, 2001.
- [27] T. Qin, K. Wu, and D. Xiu. Data driven governing equations approximation using deep neural networks. *Journal of Computational Physics*, 395:620–635, 2019.
- [28] M. Raissi, P. Perdikaris, and G. E. Karniadakis. Multistep neural networks for data-driven discovery of nonlinear dynamical systems. *arXiv preprint arXiv:1801.01236*, 2018.
- [29] R. Rico-Martinez and I. G. Kevrekidis. Continuous time modeling of nonlinear systems: A neural network-based approach. In *IEEE International Conference on Neural Networks*, pages 1522–1525. IEEE, 1993.
- [30] H. Schaeffer, G. Tran, and R. Ward. Extracting sparse high-dimensional dynamics from limited data. *SIAM Journal on Applied Mathematics*, 78(6):3279–3295, 2018.
- [31] H. Schaeffer, G. Tran, R. Ward, and L. Zhang. Extracting structured dynamical systems using sparse optimization with very few samples. *Multiscale Modeling & Simulation*, 18(4):1435–1461, 2020.

- [32] S. Terakawa and T. Yaguchi. Modeling error and nonuniqueness of the continuous-time models learned via runge–kutta methods. *Mathematics*, 12(8):1190, 2024.
- [33] P. R. Vlachas, W. Byeon, Z. Y. Wan, T. P. Sapsis, and P. Koumoutsakos. Data-driven forecasting of high-dimensional chaotic systems with long short-term memory networks. *Proceedings of the Royal Society A: Mathematical, Physical and Engineering Sciences*, 474(2213):20170844, 2018.
- [34] C. Wehmeyer and F. Noé. Time-lagged autoencoders: Deep learning of slow collective variables for molecular kinetics. *The Journal of chemical physics*, 148(24), 2018.
- [35] X. Xie, G. Zhang, and C. G. Webster. Non-intrusive inference reduced order model for fluids using deep multistep neural network. *Mathematics*, 7(8):757, 2019.
- [36] E. Yeung, S. Kundu, and N. Hodas. Learning deep neural network representations for koopman operators of nonlinear dynamical systems. In *2019 American Control Conference (ACC)*, pages 4832–4839. IEEE, 2019.
- [37] L. Zhang and H. Schaeffer. On the convergence of the sindy algorithm. *Multi-scale Modeling & Simulation*, 17(3):948–972, 2019.
- [38] A. Zhu, P. Jin, B. Zhu, and Y. Tang. On numerical integration in neural ordinary differential equations. In *International Conference on Machine Learning*, pages 27527–27547. PMLR, 2022.
- [39] A. Zhu, S. Wu, and Y. Tang. Error analysis based on inverse modified differential equations for discovery of dynamics using linear multistep methods and deep learning. *SIAM Journal on Numerical Analysis*, 62(5):2087–2120, 2024.

6 Appendix

6.1 Coefficients of Linear Multistep Methods

Here we provide a table that summarizes the coefficients of the Linear Multistep Methods (LMMs) analyzed in this article. Recall the general form of an LMM:

$$\sum_{j=0}^k \alpha_j z_{n+j} = \lambda h \sum_{j=0}^k \beta_j z_{n+j}, \quad \alpha_k = 1,$$

where α_j and β_j are the method-specific coefficients. The following table includes Adams–Moulton methods (AM2, AM3), Adams–Bashforth methods (AB2, AB3), Backward Differentiation Formulas (BDF2), and the Leap–Frog scheme.

Table 7: Monic coefficients of the LMMs considered in this article.

| Method | k | α_j (from $j = 0$ to k) | β_j (from $j = 0$ to k) |
|-----------|-----|-----------------------------------|---|
| AM2 | 1 | $-1, 1$ | $\frac{1}{2}, \frac{1}{2}$ |
| AM3 | 2 | $-1, 0, 1$ | $\frac{-1}{12}, \frac{2}{3}, \frac{5}{12}$ |
| AB2 | 2 | $0, -1, 1$ | $\frac{-1}{2}, \frac{3}{2}, 0$ |
| AB3 | 3 | $0, 0, -1, 1$ | $\frac{-5}{12}, \frac{-16}{12}, \frac{23}{12}, 0$ |
| BDF2 | 2 | $\frac{1}{3}, \frac{-4}{3}, 1$ | $0, 0, \frac{2}{3}$ |
| Leap-Frog | 2 | $-1, 0, 1$ | $0, 1, 0$ |

6.2 Consistency and order of convergence

We report below the consistency of the optimal solution to the learning problem: the theorems in this section show $\hat{\lambda} \rightarrow \lambda$ as $h \rightarrow 0$ for one-step and linear multistep methods.

6.2.1 One-step methods

Following Lemma 2.1,

$$e^{\lambda h} = 1 + \lambda h + \frac{(\lambda h)^2}{2!} + \dots = p(\hat{\lambda} h),$$

and we can determine the convergence rate of $\hat{\lambda}$ to λ as the step size $h \rightarrow 0$.

Theorem 6.1. *The order of convergence of $\hat{\lambda}$ in $\{z \in \mathbb{C}, |z| \leq 1\}$ to λ as $h \rightarrow 0$ corresponds to the order of the one-step numerical scheme used in generating z_n in (13). We have the following:*

- (The Forward Euler method) $|\hat{\lambda} - \lambda| = \mathcal{O}(h)$,
- (The k -th Runge-Kutta method) $|\hat{\lambda} - \lambda| = \mathcal{O}(h^k)$,
- (The Backward Euler method) $|\hat{\lambda} - \lambda| = \mathcal{O}(h)$,
- (The implicit trapezoidal method) $|\hat{\lambda} - \lambda| = \mathcal{O}(h^2)$.

Proof. **[Forward Euler, and k -th Runge-Kutta method]**

Due to the multiple roots in k -th Runge-Kutta methods, we focus the root with $|\hat{\lambda}h| \leq 1$. Consider the Taylor expansion of $e^{\lambda h}$, we have :

$$e^{\lambda h} = \sum_{j=0}^k \frac{(\lambda h)^j}{j!} + R(\lambda h) = p(\lambda h) + R(\lambda h),$$

where $|R(\lambda h)| = \mathcal{O}(h^{k+1})$.

Next, following the equation

$$e^{\lambda h} = p(\hat{\lambda}h),$$

and we know that $|p'(\eta)| \neq 0$ where $|\eta| \leq 1$, hence

$$\begin{aligned} p(\hat{\lambda}h) &= p(\lambda h) + R(\lambda h) \\ \Rightarrow c|\hat{\lambda}h - \lambda h| &\leq |p(\hat{\lambda}h) - p(\lambda h)| \leq |R(\lambda h)| \leq \mathcal{O}(h^{k+1}), \quad \text{for } c > 0. \end{aligned}$$

[Backward Euler, Implicit Trapezoidal rule]

For the implicit Trapezoidal rule

$$\begin{aligned} e^{\lambda h} &= \frac{1 + \hat{\lambda}h/2}{1 - \hat{\lambda}h/2} \implies \hat{\lambda}h = 2 \frac{e^{\lambda h} - 1}{(e^{\lambda h} + 1)} = \lambda h + \mathcal{O}(h^3), \\ \implies |\lambda h - \hat{\lambda}h| &= \mathcal{O}(h^3). \end{aligned}$$

On the other hand, for the Backward Euler:

$$\begin{aligned} e^{\lambda h} &= \frac{1}{1 - \hat{\lambda}h} \implies 1 - \hat{\lambda}h = e^{-\lambda h} = \sum_{n=0}^{\infty} \frac{(-\lambda h)^n}{n!} \\ \implies |\lambda h - \hat{\lambda}h| &= \mathcal{O}(h^2). \end{aligned}$$

□

6.2.2 Linear Multistep Methods

Given the relationship of the learned dynamic to the true dynamic stated in Lemma 3.1:

$$\hat{\lambda}h = \frac{\rho(e^{\lambda h})}{\kappa(e^{\lambda h})}.$$

The asymptotic expansion of $\frac{\rho(e^{\lambda h})}{\kappa(e^{\lambda h})}$ provides the convergence rate of $\hat{\lambda}$ to λ as $h \rightarrow 0$. For instance, while the Leap-Frog scheme is considered to generate predictions z_n in (21), the learned dynamic $\hat{\lambda}h$ follows the following equation:

$$\begin{aligned} \hat{\lambda}h &= \frac{e^{2\lambda h} - 1}{2e^{\lambda h}} = \frac{e^{\lambda h} - e^{-\lambda h}}{2}, \\ \Rightarrow \hat{\lambda}h &= \lambda h + \mathcal{O}(h^3), \\ \Rightarrow |\hat{\lambda} - \lambda| &= \mathcal{O}(h^2). \end{aligned}$$

Theorem 6.2. *The order of convergence of $\hat{\lambda}$ to λ as $h \rightarrow 0$ corresponds to the order of the linear multistep method used in generating z_n in (13). We have the following:*

- (*k*-step Adams-Moulton methods) $|\lambda h - \hat{\lambda}h| = \mathcal{O}(h^{k+1})$,
- (*k*-step Adams-Bashforth methods) $|\lambda h - \hat{\lambda}h| = \mathcal{O}(h^{k+2})$,
- (*The Leap-Frog scheme*) $|\lambda h - \hat{\lambda}h| = \mathcal{O}(h^3)$.

Proof. These conclusions follow directly from the Taylor expansion of $\frac{\rho(e^{\lambda h})}{\kappa(e^{\lambda h})}$. \square

6.3 Proofs of theorems in Section 2

6.3.1 Conservative cases

[Forward Euler]

Proof. Proof of Corollary 2.1.

Consider using the Forward Euler method as the numerical integrator in (13), where $p(\xi) = 1 + \xi$. The conclusion in Lemma 2.1 shows that

$$p(\hat{\lambda}h) = e^{\lambda h} \Rightarrow (1 + \hat{\lambda}h) = e^{\lambda h}. \quad (33)$$

Aligning the real part and the imaginary part of (33),

$$\begin{aligned} 1 + \operatorname{Re}(\hat{\lambda}h) &= \cos(\lambda h) \\ \operatorname{Im}(\hat{\lambda}h) &= \sin(\lambda h). \end{aligned}$$

First notice $1 + \operatorname{Re}(\hat{\lambda}h) = \cos(\lambda h)$ provides $\operatorname{Re}(\hat{\lambda}h) < 0$. Next, following the assumption $\operatorname{Im}(\lambda h) \in (-\pi, \pi)$, we conclude $\operatorname{sign}(\operatorname{Im}(\hat{\lambda}h)) = \operatorname{sign}(\sin(\lambda h)) = \operatorname{sign}(\operatorname{Im}(\lambda h))$. \square

Proof. Proof of Corollary 2.2.

We first prove the existence and uniqueness of a $\hat{\lambda}h$ satisfies $p(\hat{\lambda}h) = e^{\lambda h}$ and $|\hat{\lambda}h| \leq 1$ where $h > 0$ is prescribed

- unconditional **[RK2]**,
- $|1 - e^{\lambda h}| \leq \frac{1}{6}$ **[RK3]**,

[RK2] We first show that if $h > 0$ satisfies $2|1 - e^{\lambda h}| < 1$ then there exists a unique solution $\hat{\lambda}h$ of $1 + \xi + \frac{\xi^2}{2} = e^{\lambda h}$ with $|\hat{\lambda}h| < 1$. The proof is directly from Vieta's formula:

$$\begin{aligned} z_1 + z_2 &= -2, \\ z_1 z_2 &= 2(1 - e^{\lambda h}), \end{aligned}$$

where z_1, z_2 are solutions of $1 + \xi + \frac{\xi^2}{2} = e^{\lambda h}$. Therefore, we have, without loss of generality, $\operatorname{Re}(z_1) < -1 \Rightarrow |z_1| > 1$. Following the assumption $h > 0$ and satisfies $2|1 - e^{\lambda h}| < 1$, we have $|z_2| < |z_1||z_2| \leq 1$. Next, we show $z_2 = \hat{\lambda}h$ has the properties containing $\operatorname{Re}(\hat{\lambda}) < 0$, and $\operatorname{sign}(\operatorname{Im}(\hat{\lambda}h)) = \operatorname{sign}(\operatorname{Im}(\lambda h))$. Expanding the real part and the imaginary part of $1 + \hat{\lambda}h + \frac{(\hat{\lambda}h)^2}{2} = e^{\lambda h}$:

$$\begin{aligned} 1 + \operatorname{Re}(\hat{\lambda}h) + \frac{\operatorname{Re}(\hat{\lambda}h)^2 - \operatorname{Im}(\hat{\lambda}h)^2}{2} &= \cos(\lambda h), \\ \operatorname{Im}(\hat{\lambda}h) + \operatorname{Re}(\hat{\lambda}h)\operatorname{Im}(\hat{\lambda}h) &= \sin(\lambda h). \end{aligned} \tag{34}$$

If the solution $\hat{\lambda}h$ has non-negative real part, then

$$1 - \frac{\operatorname{Im}(\hat{\lambda}h)^2}{2} \leq 1 + \operatorname{Re}(\hat{\lambda}h) + \frac{\operatorname{Re}(\hat{\lambda}h)^2 - \operatorname{Im}(\hat{\lambda}h)^2}{2} = \cos(\lambda h),$$

and with $\text{Im}(\hat{\lambda}h) + \text{Re}(\hat{\lambda}h) \text{Im}(\hat{\lambda}h) = \sin(\lambda h)$ we have

$$\begin{aligned} & \left(1 - \frac{\text{Im}(\hat{\lambda}h)^2}{2}\right)^2 + \left(1 + \text{Re}(\hat{\lambda}h)\right)^2 \text{Im}(\hat{\lambda}h)^2 < 1 \\ \Rightarrow & \left(1 - \frac{\text{Im}(\hat{\lambda}h)^2}{2}\right)^2 + \text{Im}(\hat{\lambda}h)^2 < 1 \quad (\text{this followed by assuming } \text{Re}(\hat{\lambda}h) \geq 0) \\ \Rightarrow & 1 + \frac{\text{Im}(\hat{\lambda}h)^4}{4} \leq 1 \Rightarrow \text{Im}(\hat{\lambda}h) = 0. \end{aligned}$$

Thus, $\hat{\lambda}$ is a real number. Revisiting (34) and we find $\sin(\lambda h) = 0$, which contradicts the setting that λ can be an arbitrary purely complex number. Therefore we show $\text{Re}(\hat{\lambda}) < 0$.

Finally, by examining the second equation in (34) and applying $\text{Re}(\hat{\lambda}h) > -1$ we have $(1 + \text{Re}(\hat{\lambda}h)) > 0$

$$\text{sign}(\text{Im}(\hat{\lambda}h)) = \text{sign}(\sin(\lambda h)). \quad (35)$$

We conclude that if h satisfies $\text{Im}(\lambda h) \in (-\pi, \pi)$, then $\text{sign}(\text{Im}(\hat{\lambda}h)) = \text{sign}(\text{Im}(\lambda h))$.

[RK3] We first show that if $h > 0$ satisfies $6|1 - e^{\lambda h}| < 1$ then the solutions $\hat{\lambda}h$ of

$$1 + \xi + \frac{\xi^2}{2} + \frac{\xi^3}{6} = e^{\lambda h}, \quad |\xi| < 1, \quad (36)$$

contain a positive real part. Since the equation

$$\left|1 + \xi + \frac{\xi^2}{2} + \frac{\xi^3}{6}\right| = 1,$$

intersects with the imaginary axis at $(0, 0)$, $(0, \pm\sqrt{3})$, implies the solutions of $1 + \xi + \frac{\xi^2}{2} + \frac{\xi^3}{6} = e^{\lambda h}$ has non-negative real part while prescribing the solution's module should less than 1. Next, we show if the step size $h > 0$ satisfies $6|1 - e^{\lambda h}| < 1$, then the solution of (36) is unique. Recalling Vieta's formula:

$$\begin{aligned} z_1 + z_2 + z_3 &= -3 \\ z_1 z_2 + z_2 z_3 + z_1 z_3 &= 6 \\ z_1 z_2 z_3 &= -6(1 - e^{\lambda h}). \end{aligned}$$

where z_1, z_2, z_3 are solutions of $1 + \xi + \frac{\xi^2}{2} + \frac{\xi^3}{6} = e^{\lambda h}$. Therefore, we have, without loss of generality, $\operatorname{Re}(z_1) < -1$, and $|z_1| > 1$. Following the assumption $h > 0$ and satisfies $6|1 - e^{\lambda h}| < 1$, we have $|z_2||z_3| < |z_1||z_2||z_3| \leq 1$. If both z_2 and z_3 satisfy $|z_2|, |z_3| \leq 1$, by the positivity property we derived for solutions of (36),

$$\operatorname{Re}(z_1) \leq \operatorname{Re}(z_1) + \operatorname{Re}(z_2) + \operatorname{Re}(z_3) = -3$$

which contradicts the fact that the graph

$$\left|1 + \xi + \frac{\xi^2}{2} + \frac{\xi^3}{6}\right| = 1,$$

contains in $[-3, 1] \times [-3i, 3i]$. Therefore, we conclude the solution's uniqueness property of (36) while satisfying the condition $6|1 - e^{\lambda h}| < 1$. Next, denoting $z_3 = \hat{\lambda}h$ as the solution of (36), and show its rotation direction by comparing the imaginary part of $e^{\lambda h} = p(\hat{\lambda}h)$:

$$\sin(\operatorname{Im}(\lambda h)) = \operatorname{Im}(\hat{\lambda}h) \left(\frac{(\operatorname{Re}(\hat{\lambda}h))^2}{2} + (\operatorname{Re}(\hat{\lambda}h)) + 1 - \frac{(\operatorname{Im}(\hat{\lambda}h))^2}{6} \right).$$

Since the solutions we currently focus on lie in $|z| < 1$ moreover possess $(\operatorname{Im}(\hat{\lambda}h))^2 \in [0, 3]$ making $\left(\frac{(\operatorname{Re}(\hat{\lambda}h))^2}{2} + (\operatorname{Re}(\hat{\lambda}h)) + 1 - \frac{(\operatorname{Im}(\hat{\lambda}h))^2}{6} \right) > 0$. We conclude when $\operatorname{Im}(\lambda h) \in (-\pi, \pi)$, then $\operatorname{sign}(\operatorname{Im}(\lambda h)) = \operatorname{sign}(\operatorname{Im}(\hat{\lambda}h))$. \square

Proof. Proof of Corollary 2.3.

[Backward Euler] Assuming the step size $h > 0$ satisfies

$$\operatorname{Im}(\lambda h) \in (-\pi, \pi) \tag{37}$$

We aim to show that the solution $\hat{\lambda}h$ of

$$\frac{1}{1 - \hat{\lambda}h} = e^{\lambda h}, \tag{38}$$

contains $\operatorname{Re}(\hat{\lambda}) > 0$ and $\operatorname{sign}(\operatorname{Im}(\lambda h)) = \operatorname{sign}(\operatorname{Im}(\hat{\lambda}h))$. To reveal these properties, we compare the real part and the imaginary part of (38):

$$\begin{aligned} 1 - \operatorname{Re}(\hat{\lambda}h) &= \cos(-\lambda h), \\ \operatorname{Im}(\hat{\lambda}h) &= \sin(-\lambda h). \end{aligned}$$

It is clear to realize $\operatorname{Re}(\hat{\lambda}h) > 0$ and $\operatorname{sign}(\operatorname{Im}(\lambda h)) = \operatorname{sign}(\operatorname{Im}(\hat{\lambda}h))$

[Implicit trapezoidal rule] Analogously, we analyze the case considering the implicit trapezoidal rule. Assuming the step size $h > 0$ satisfies

$$\text{Im}(\lambda h) \in (-\pi, \pi) \quad (39)$$

To reveal that the solution $\hat{\lambda}h$ of

$$\frac{1 + 1/2\hat{\lambda}h}{1 - 1/2\hat{\lambda}h} = e^{\lambda h} \Rightarrow \hat{\lambda}h = 2\frac{1 - e^{\lambda h}}{1 + e^{\lambda h}}$$

contains zero real part and $\text{sign}(\text{Im}(\lambda h)) = \text{sign}(\text{Im}(\hat{\lambda}h))$.

Since

$$\hat{\lambda}h = 2\frac{1 - e^{\lambda h}}{1 + e^{\lambda h}} = 2\frac{e^{-\lambda h/2} - e^{\lambda h/2}}{e^{-\lambda h/2} + e^{\lambda h/2}},$$

and we assume λ is a purely imaginary number, $\text{Re}(\hat{\lambda}h) = 2 \text{Re}\left(\frac{e^{-\lambda h/2} - e^{\lambda h/2}}{e^{-\lambda h/2} + e^{\lambda h/2}}\right) = 0$.

In addition,

$$\text{Im}(\hat{\lambda}h) = 2 \text{Im}\left(\frac{e^{-\lambda h/2} - e^{\lambda h/2}}{e^{-\lambda h/2} + e^{\lambda h/2}}\right) = 4 \tan\left(\frac{\text{Im}(\lambda h)}{2}\right).$$

By the assumption that $\text{Im}(\lambda h) \in (-\pi, \pi)$ we conclude $\text{sign}(\text{Im}(\lambda h)) = \text{sign}(\text{Im}(\hat{\lambda}h))$ and complete our proof. \square

6.3.2 Dissipative cases

[Forward Euler]

Proof. Proof of Corollary 2.4 To show the real part of the learned dynamic $\hat{\lambda}$ is negative, we recall Lemma 2.1 that

$$1 > |e^{\lambda h}| = |1 + \hat{\lambda}h|.$$

The solution to the inequality lies inside the stability region, which is located entirely on the left-hand side of the complex plane, indicating a negative real part.

The analysis of the sign of $\text{Im}(\hat{\lambda})$ follows the same strategy as the proofs in the conservative dynamic setting. Consider $\text{Im}(\lambda h) \in (-\pi, \pi)$, then the imaginary part of the equation

$$e^{\lambda h} = (1 + \hat{\lambda}h)$$

shows that

$$\sin(\text{Im}(\lambda h)) = \text{Im}(\hat{\lambda}h).$$

This asserts the sign of $\text{Im}(\hat{\lambda})$ is equal to the sign of $\text{Im}(\lambda)$. \square

Proof. **Proof of Corollary 2.5**

[RK2] We begin by demonstrating that there is a unique solution that satisfies

$$1 + \hat{\lambda}h + \frac{(\hat{\lambda}h)^2}{2} = e^{\lambda h}, \quad |\hat{\lambda}h| \leq 1.$$

Let z_1, z_2 be the solutions of (14) with $p(z) = 1 + z + \frac{z^2}{2}$. By Vieta's formula,

$$\begin{aligned} z_1 + z_2 &= -2 \\ z_1 z_2 &= 2(1 - e^{\lambda h}), \end{aligned}$$

we know that there is a root, say z_1 , with $\text{Re}(z_1) < -1$, thus $|z_1| > 1$. In addition, if h satisfies $|2(1 - e^{\lambda h})| < 1$, then

$$|z_2| < |z_1| |z_2| = |2(1 - e^{\lambda h})| \leq 1.$$

Next, we show that the real part of the solution is negative. This fact can be deduced from the fact that the stability region of the RK2 method lies on the left-hand side of the complex plane.

Finally, we investigate the direction of phase rotation. Following by aligning the imaginary part of

$$1 + \hat{\lambda}h + \frac{(\hat{\lambda}h)^2}{2} = e^{\lambda h}.$$

Through direct computation,

$$\begin{aligned} \text{Im}(\hat{\lambda}h) + \frac{2(\text{Im}(\hat{\lambda}h) \text{Re}(\hat{\lambda}h))}{2} &= \sin(\lambda h), \\ \Rightarrow \text{Im}(\hat{\lambda}h)(1 + \text{Re}(\hat{\lambda}h)) &= \sin(\lambda h) \end{aligned}$$

Since we focus $|\hat{\lambda}h| < 1$, we have $1 + \text{Re}(\hat{\lambda}h) > 0$. Consequently, as $\text{Im}(\lambda h) \in (-\pi, \pi)$

$$\text{sign}(\text{Im}(\hat{\lambda}h)) = \text{sign}(\text{Im}(\lambda h))$$

[RK3] We first claim that if $|e^{\lambda h}| \leq \sqrt{\frac{8}{9}}$ then all the roots of the following equation:

$$1 + z + \frac{z^2}{2!} + \frac{z^3}{3!} = e^{\lambda h} \tag{40}$$

follow a negative real part.

Note that

$$\{z \in \mathbb{C}, |p(z)| = c_1\} \subset \{z \in \mathbb{C}, |p(z)| \leq c_2\}, \quad c_1 < c_2.$$

Therefore, we only need to find a value c such that the curve $\{z \in \mathbb{C}, |p(z)| = c\}$ is tangent to the imaginary axis.

Expanding the real and imaginary parts of the equation:

$$|e^{\lambda h}|^2 = \left| 1 + \hat{\lambda}h + \frac{(\hat{\lambda}h)^2}{2!} + \frac{(\hat{\lambda}h)^3}{3!} \right|^2. \quad (41)$$

We target the location where the level set (41) tangents to the imaginary axis by considering the implicit derivative of $\text{Re}(\hat{\lambda}h)$ to $\text{Im}(\hat{\lambda}h)$ at $\text{Re}(\hat{\lambda}h) = 0$:

$$\begin{aligned} \frac{\text{Im}(\hat{\lambda}h)(\text{Im}(\hat{\lambda}h)^4 - 2\text{Im}(\hat{\lambda}h)^2)}{-\text{Im}(\hat{\lambda}h)^4 - 12} &= 0, \\ \Rightarrow \text{Im}(\hat{\lambda}h) &= 0, \pm\sqrt{2}. \end{aligned}$$

We discard $\text{Im}(\hat{\lambda}h) = 0$ as $h > 0$ implies $|e^{\lambda h}| > 0$. Substituting $(0, \pm\sqrt{2})$ back into (41), we find that

$$|e^{\lambda h}| = \frac{8}{9}.$$

Consequently, we conclude that if h satisfies $|e^{\lambda h}| < \frac{8}{9}$, then all the roots of (40) contain negative real part.

Next, we show that there is at least one solution that satisfies the following equation:

$$1 + z + \frac{z^2}{2!} + \frac{z^3}{3!} = e^{\lambda h}, \quad |z| \leq \delta,$$

where δ satisfies $\frac{6 - \delta^2}{2\delta} \geq \sqrt{12.5}$. Applying Vieta's formulas:

$$\begin{aligned} z_1 + z_2 + z_3 &= -3 \\ z_1z_2 + z_2z_3 + z_1z_3 &= 6 \\ z_1z_2z_3 &= 6(1 - e^{\lambda h}), \end{aligned}$$

where z_1, z_2, z_3 are solutions of (14) with $p(z) = 1 + z + \frac{z^2}{2} + \frac{z^3}{3!}$.

From the Vieta's formulas, we know that $z_1 + z_2 + z_3 = -3$, showing there is a root, say z_1 , has $\text{Re}(z_1) < -1$.

Next, we claim that at least one z exists such that $|z| \leq \delta$. We also know from Vieta's formula:

$$\begin{aligned} z_1 z_2 z_3 &= 6(1 - e^{\lambda h}) \\ \Rightarrow |z_2||z_3| &< |z_1||z_2||z_3| = 6|(1 - e^{\lambda h})| \leq \delta^2. \end{aligned}$$

Therefore we have either z_2 or z_3 satisfies $|z| < \delta$.

Finally, we show the uniqueness. If z_2, z_3 both satisfy $|z| \leq \delta$ then we have

$$\begin{aligned} 6 &= |z_1 z_2 + z_2 z_3 + z_1 z_3| \leq |z_1||z_2| + |z_2||z_3| + |z_1||z_3| \leq \delta^2 + 2\delta|z_1| \\ \Rightarrow \frac{6 - \delta^2}{2\delta} &\leq |z_1|. \end{aligned}$$

Since the step size h must satisfy

$$|e^{\lambda h}| \leq \sqrt{\frac{8}{9}},$$

we consider the region

$$\left\{ z \in \mathbb{C} \left| \left| 1 + z + \frac{z^2}{2} + \frac{z^3}{6} \right| \leq \sqrt{\frac{8}{9}} \right\} \subset [-2.5, 0] \times [-2.5i, 2.5i].$$

Hence, if

$$\frac{6 - \delta^2}{2\delta} > \sqrt{12.5} \quad \Rightarrow \quad |z_1| > \sqrt{12.5},$$

then z_1 lies outside the actual stability region, leading to a contradiction.

The discussion regarding the sign of $\text{Im}(\hat{\lambda})$ is similar to the argument presented in the proof of Theorem 2.2. \square

Proof. **Proof of Corollary 2.6**

[Backward Euler] First, we examine the real part of $\hat{\lambda}$.

For the Backward Euler case, (14) gives us:

$$\begin{aligned} e^{\lambda h} &= \frac{1}{1 - \hat{\lambda}h}, \\ \Rightarrow 1 > |e^{\lambda h}| &= \left| \frac{1}{1 - \hat{\lambda}h} \right|, \\ \Rightarrow |1 - \hat{\lambda}h| &> 1. \end{aligned}$$

The sign of the real part of $\hat{\lambda}$ is indeterminate because when the level curve $\{z \in \mathbb{C}, |1 - z| = c\}$ has $c > 1$, it will include a portion on the left-hand side of the complex plane, making the analysis inconclusive.

[Implicit trapezoidal method] From (14), we have:

$$\begin{aligned} e^{\lambda h} &= \frac{1 + \frac{1}{2}\hat{\lambda}h}{1 - \frac{1}{2}\hat{\lambda}h}, \\ \Rightarrow 1 > |e^{\lambda h}| &= \left| \frac{1 + \frac{1}{2}\hat{\lambda}h}{1 - \frac{1}{2}\hat{\lambda}h} \right|, \\ \Rightarrow \left| 1 + \frac{1}{2}\hat{\lambda}h \right| &< \left| 1 - \frac{1}{2}\hat{\lambda}h \right|, \\ \Rightarrow \operatorname{Re}(\hat{\lambda}h) &< 0. \end{aligned}$$

The analysis of the sign of $\operatorname{Im}(\hat{\lambda}h)$ is identical to the discussion in Theorem 2.3. □

6.4 Noisy data Theorem 2.5

Proof. (i) Since $\hat{\lambda}$ is the global minimizer of the noise-free optimization problem, by Lemma 2.1, we have $p(\hat{\lambda}h)^k Z_0 = Z_0 e^{\lambda h k}$. Also

$$p(\lambda^*h)^k Z_0 - Z_0 e^{\lambda h k} = [p(\hat{\lambda}h)^k - p(\lambda^*h)^k] Z_0$$

The polynomial $p^k(\xi)$ is an analytic function – by the mean value theorem, there exist u and v on the line segment, connecting λ^*h and $\hat{\lambda}h$ on the complex plane, such that

$$(p(\lambda^*h))^k - (p(\hat{\lambda}h))^k = [\operatorname{Re}(kp(u)^{k-1}p'(u)) + i \operatorname{Im}(kp(v)^{k-1}p'(v))] (\lambda^*h - \hat{\lambda}h).$$

Without loss of generality, we assume that $\lambda^* \neq \hat{\lambda}$ (otherwise, there is nothing to prove). This means $\operatorname{Re}(kp(u)^{k-1}p'(u)) + i \operatorname{Im}(kp(v)^{k-1}p'(v)) \neq 0$ and

$$\left| (\lambda^*h - \hat{\lambda}h) Z_0 \right| = \frac{|p(\lambda^*h)^k Z_0 - Z_0 e^{\lambda h k}|}{|\operatorname{Re}(kp(u)^{k-1}p'(u)) + i \operatorname{Im}(kp(v)^{k-1}p'(v))|}. \quad (42)$$

(ii) Recall that $\hat{\lambda}$ is the minimizer of the objective function $L(\lambda)$ when data has no noise; i.e.

$$L(\hat{\lambda}) = \frac{1}{N} \sum_{k=1}^N |\epsilon_k - p(\hat{\lambda}h)^k \epsilon_0|^2.$$

So

$$L(\lambda^*) = \frac{1}{N} \sum_{k=1}^N \underbrace{|e^{\lambda h k} Z_0 + \epsilon_k - (p(\lambda^* h)^k Z_0 + p(\lambda^* h)^k \epsilon_0)|^2}_{A_k} \leq \frac{1}{N} \sum_{k=1}^N |\epsilon_k - p(\hat{\lambda} h)^k \epsilon_0|^2.$$

We want to derive an upper bound for the term $|e^{\lambda h k} Z_0 - p(\lambda^* h)^k Z_0|$. Since

$$|e^{\lambda h k} Z_0 - p(\lambda^* h)^k Z_0|^2 + |\epsilon_k - p(\lambda^* h)^k \epsilon_0|^2 - 2B_k \leq A_k,$$

where

$$B_k := |e^{\lambda h k} Z_0 - p(\lambda^* h)^k Z_0| |\epsilon_k - p(\lambda^* h)^k \epsilon_0|.$$

Therefore, we have

$$|e^{\lambda h k} Z_0 - p(\lambda^* h)^k Z_0|^2 + |\epsilon_k - p(\lambda^* h)^k \epsilon_0|^2 \leq |\epsilon_k - p(\hat{\lambda} h)^k \epsilon_0|^2 + 2B_k.$$

By the Cauchy-Schwarz inequality, we have

$$\sum_{k=1}^N B_k \leq \sqrt{\sum_{k=1}^N |e^{\lambda h k} Z_0 - p(\lambda^* h)^k Z_0|^2} \sqrt{\sum_{k=1}^N |\epsilon_k - p(\lambda^* h)^k \epsilon_0|^2}.$$

Thus,

$$\begin{aligned} & \sum_{k=1}^N |e^{\lambda h k} Z_0 - p(\lambda^* h)^k Z_0|^2 + |\epsilon_k - p(\lambda^* h)^k \epsilon_0|^2 \\ & \leq \sum_{k=1}^N |\epsilon_k - p(\hat{\lambda} h)^k \epsilon_0|^2 + 2 \sqrt{\sum_{k=1}^N |e^{\lambda h k} Z_0 - p(\lambda^* h)^k Z_0|^2} \sqrt{\sum_{n=1}^N |\epsilon_k - p(\lambda^* h)^k \epsilon_0|^2} \\ & \leq \sum_{k=1}^N |\epsilon_k - p(\hat{\lambda} h)^k \epsilon_0|^2 + \delta \sum_{k=1}^N |e^{\lambda h k} Z_0 - p(\lambda^* h)^k Z_0|^2 + \frac{1}{\delta} \sum_{n=1}^N |\epsilon_k - p(\lambda^* h)^k \epsilon_0|^2, \end{aligned}$$

for any $\delta > 0$. Picking $\delta = 1/2$,

$$\implies \frac{1}{2} \sum_{k=1}^N |e^{\lambda h k} Z_0 - p(\lambda^* h)^k Z_0|^2 \leq \sum_{k=1}^N |\epsilon_k - p(\hat{\lambda} h)^k \epsilon_0|^2 + \sum_{n=1}^N |\epsilon_k - p(\lambda^* h)^k \epsilon_0|^2.$$

By Theorem 2.2, for dissipative systems, $\hat{\lambda} h$ is always confined in the stability region of the given method; i.e., $|p(\hat{\lambda} h)| < 1$. Then by the given hypothesis that $|p(\lambda^* h)| \leq M$, we have

$$\left(\sum_{k=1}^N |e^{\lambda h k} Z_0 - p(\lambda^* h)^k Z_0|^2 \right) \leq \frac{\max(1, M^{2k})}{2} \sum_{k=1}^N (|\epsilon_k| + |\epsilon_0|)^2.$$

Finally, bringing this inequality into (42), we conclude that

$$\left| \lambda^* h - \hat{\lambda} h \right|^2 \leq C \sigma^2$$

for some constant C depending on Z_0 and $p(\lambda^* h)$. \square

6.5 Proof of theorems in Section 3

6.5.1 Conservative cases

[AM3 and AB methods]

Proof. Proof of Corollary 3.1 and 3.2

We demonstrate the proof for the case of using AB3, as the other cases follow the same strategy. The characteristic polynomials corresponding to the AB3 method are given by:

$$\rho(\xi) = \xi^3 - \xi^2, \quad \kappa(\xi) = \frac{23}{12}\xi^2 - \frac{16}{12}\xi + \frac{5}{12}.$$

The learned dynamic follows:

$$\begin{aligned} \hat{\lambda} h &= \frac{\rho(e^{\lambda h})}{\kappa(e^{\lambda h})} = \frac{e^{3\lambda h} - e^{2\lambda h}}{\frac{23}{12}e^{2\lambda h} - \frac{16}{12}e^{\lambda h} + \frac{5}{12}} \\ &= 12 \frac{e^{3\lambda h} - e^{2\lambda h}}{23e^{2\lambda h} - 16e^{\lambda h} + 5}. \end{aligned}$$

By expressing $e^{\lambda h} = \cos(\text{Im}(\lambda h)) + i \sin(\text{Im}(\lambda h))$, and denote $C = \frac{12}{|23e^{2\lambda h} - 16e^{\lambda h} + 5|^2}$, we have:

$$\begin{cases} \text{Re}(\hat{\lambda} h) = 8C(-1 + 10 \cos(\text{Im}(\lambda h))) \sin^4\left(\frac{\text{Im}(\lambda h)}{2}\right), \\ \text{Im}(\hat{\lambda} h) = C \sin(\text{Im}(\lambda h))(22 - 21 \cos(\text{Im}(\lambda h)) + 5 \cos(2 \text{Im}(\lambda h))). \end{cases}$$

The sign of $\text{Re}(\hat{\lambda} h)$ is determined by the sign of $-1 + 10 \cos(\text{Im}(\lambda h))$, since $22 - 21 \cos(\text{Im}(\lambda h)) + 5 \cos(2 \text{Im}(\lambda h))$ is always positive.

On the other hand, $\text{sign}(\text{Im}(\hat{\lambda} h)) = \text{sign}(\text{Im}(\lambda h))$ due to the fact that $\text{Im}(\lambda h) \in (-\pi, \pi)$. \square

6.6 Noisy data Theorem 3.3

The theorem can be proven using the same strategy employed in the proof of Theorem 2.5.